Lithos 318–319 (2018) 176–193

Contents lists available at ScienceDirect

Lithos

journal homepage: www.elsevier.com/locate/lithos

Petrogenesis and geodynamic significance of the ~850 Ma Dongling A-type granites in South China

Si-Fang Huang, Wei Wang *, Jun-Hong Zhao, Jian-Ping Zheng

State Key Laboratory of Geological Processes and Mineral Resources, School of Earth Science, China University of Geosciences, Wuhan 430074, China

ARTICLE INFO

Article history:
Received 30 March 2018
Accepted 11 August 2018
Available online 16 August 2018

Keywords:
Dongling A-type granites
Petrogenesis
Geodynamic setting
Neoproterozoic
South China Block

ABSTRACT

The ongoing controversy on the timing of amalgamation of the Yangtze and Cathaysia Blocks (either prior to 890 Ma or later than 830 Ma) impedes a proper understanding of geological evolution of the South China Block and its role in the breakup of Rodinia supercontinent. In this study, we report ~850 Ma LA-ICP-MS zircon U—Pb ages and whole rock geochemistry of the Dongling granites from the southeastern Yangtze Block that did not receive much geoscientific attention as compared to the better-studied 830–760 Ma sedimentary and igneous rocks in the South China Block. The studied Dongling granites have high $K_2O + Na_2O$ (7.44–9.09 wt%) and low MgO (0.07–0.54 wt%) and CaO (0.16–1.21 wt%) contents. Their high $FeO^T/(FeO^T + MgO)$ (0.82–0.94) and Ga/Al (> 2.6) values and HFSE abundance (Zr + Nb + Ce + Y = 443–965 ppm) allow their grouping as A-type granite. In the chondrite normalized diagrams, these granites display right-inclined REE patterns and strong to moderate negative Eu anomalies (Eu/Eu* = 0.32–0.70). The Dongling granites have variable and negative whole-rock $\varepsilon_{Nd}(t)$ (−14.6 to −8.6) and zircon $\varepsilon_{Hf}(t)$ (−12.8 to −4.4) with Paleoproterozoic two-stage Nd (2.20–2.69 Ga) and Hf model ages (2.01–2.41 Ga). Zircon saturation parameters (T_{Zr}) suggest > 850 °C temperature and other geochemical characteristics reveal low melting pressure (> 350 to < 700 MPa) and 1.9–2.6 wt% H_2O content. Geochemical and isotopic characteristics indicate derivation of the Dongling A-type granites by partial melting of an ancient granulitic metasedimentary source, after a previous melt extraction episode. Emplacement of the Dongling A-type granites is inferred in an extensional setting following the arc-continent collision along the southeastern Yangtze Block margin. The oceanic slab continued to subduct underneath the southeastern margin of the Yangtze Block, leading to the extensive 840–820 Ma arc-related magmatism and coeval sedimentation. These arc-related igneous and sedimentary rocks indicate that the continental arc systems started from 850 Ma, and hint at the collision between the Yangtze and Cathaysia blocks after 850 Ma.

1. Introduction

It has been widely accepted that the South China Block was amalgamated during the Neoproterozoic by convergence of the Yangtze and Cathaysia Blocks along the Jiangnan Orogenic Belt (Li et al., 2009; Wang et al., 2013; Zhang et al., 2012; Zhang and Zheng, 2013; Zhao et al., 2011; Zhao and Cawood, 2012; Zheng et al., 2013). Therefore, proper understanding of the Jiangnan Orogenic Belt is crucial not only for constraining the tectonic evolution of the South China Block but also for refining the assembly and breakup history of the Rodinia supercontinent (Li et al., 2008c). The timing of amalgamation of the South China Block and its geodynamic setting are still controversial on account of diverse age constraints (Chen, 1991; Li et al., 2010a; Lyu et al., 2017; Wang et al., 2014, 2014a; Zhang et al., 2013a; Zhao et al., 2011; Zhou et al., 2002). The unresolved key issues are the secular tectonic evolution of the South China Block during ca. 890–830 Ma (Li et al., 2010b; Wang et al., 2014; Wu et al., 2006; Zhao et al., 2011; Zheng et al., 2008; Zhou et al., 2002). Some researchers suggest that the Yangtze and Cathaysia Blocks did not collide until ~830 Ma or later, and interpret that the igneous and sedimentary rocks older than 830 Ma were formed in a subduction-collision setting (Zhou et al., 2002, 2004; Wang et al., 2006, 2014, 2018a; Zhao et al., 2011; Li et al., 2013; Su et al., 2014; Zhang et al., 2015b; Zhao, 2015; Cui et al., 2017; Liu and Zhao, 2018; Huang and Wang, 2018; Xia et al., 2018). An alternative proposition envisages amalgamation of the two blocks at ~890 Ma, followed by the 850 Ma mantle plume induced continental rifting and associated Rodinia breakup (Li et al., 2003, 2010a, 2010b; Lyu et al., 2017). Despite limited outcrops, the 880–830 Ma rocks hold a key position in the Neoproterozoic geodynamics of the South China Block. In this study we present petrological, zircon U-Pb-Hf isotopic, whole rock geochemical and isotopic data on the 850 Ma A-type Dongling granites in the Jiangnan Orogenic Belt, South China (Fig. 1). The findings provide robust age constraints and offer definitive evidence for derivation of these granites by high temperature and low pressure melting of a granulitic metasedimentary source.

* Corresponding author.
E-mail address: wwz@cug.edu.cn (W. Wang).

https://doi.org/10.1016/j.lithos.2018.08.016

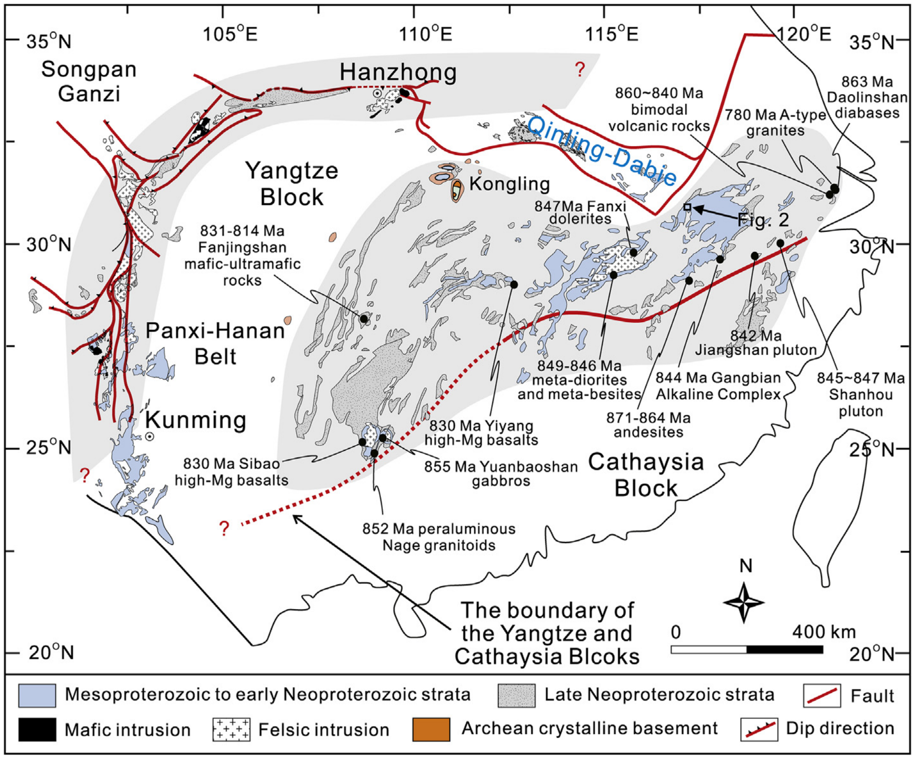

Fig. 1. Geological map showing position of Dongling Complex in the Yangtze and Cathaysia Blocks, adapted from Zhao et al. (2011), Zhao and Cawood (2012) and Zheng et al. (2013). 852 Ma peraluminous granitoids (Wu et al., 2018); 848 Ma Gangbian Alkaline Complex (Li et al., 2010b); 860–840 Ma bimodal volcanic rocks (Li et al., 2010a; Lyu et al., 2017); 849 Ma Shenwu doleritic dykes (Li et al., 2008b); 847–842 Ma Shanhou and Jiangshang pluton (Liu et al., 2015); 863 Ma Daolinshan diabases and 855 Ma Yuanbaoshan gabbros (Yao et al., 2014); 847 Ma Fanxi dolerites (Zhang et al., 2013b); 849–846 Ma meta-diorites and meta-basites (Sun et al., 2017); 830 Ma Yiyang and Sibao high-Mg basalts (Zhao and Zhou, 2013); 831–814 Ma Fanjingshan mafic-ultramafic rocks (Wang et al., 2014); 780 Ma A-type granites (Wang et al., 2010); 871–864 Ma andesites (Yao et al., 2015).

2. Geological background and sampling

The South China Block comprises the Yangtze Block in the northwest and the Cathaysia Block in the southeast, separated by the Jiangnan Orogenic Belt (Zhao and Cawood, 2012; Zheng et al., 2013). It is separated from the North China Craton by the Qinling-Dabie-Sulu Orogenic Belt in the north, from the Songpan-Gantze terrane by the Longmenshan Fault in the northwest and from the Indochina Block by the Ailaoshan-Songma suture zone in the southwest (Zhao and Cawood, 2012; Zheng et al., 2013).

The basement of the Yangtze Block is represented by sporadically exposed Archean Kongling TTG rocks in the northern part (Gao et al., 2011; Guo et al., 2014; Qiu et al., 2000), and Paleoproterozoic to early Mesoproterozoic metamorphic, sedimentary and igneous rocks along the margin of the block (Min et al., 2008; Sun et al., 2009; Yin et al., 2013; Chen et al., 2014; Wang and Zhou, 2014; Han et al., 2017; Zhou et al., 2014). These rocks are unconformably overlain by late Mesoproterozoic to early Neoproterozoic sedimentary sequences and associated magmatic rocks. These sedimentary and magmatic rocks can be further subdivided into the Jiangnan Orogenic Belt along the southeast margin and Panxi-Hannan Orogenic Belt along the western-northwestern margin of the Yangtze Block (Zhao and Cawood, 2012; Zheng et al., 2013). Within the Jiangnan Orogenic Belt, widespread Middle Neoproterozoic marine clastic sedimentary sequences, such as the Shuangqiaoshan Group in Jiangxi Province and the Sibao Group in Guangxi Province (Fig. 1), were traditionally regarded as Mesoproterozoic rocks but actually Neoproterozoic in ages (Li et al., 2016; Wang et al., 2008, 2013; Ye et al., 2007; Zhao et al., 2013; Zhou et al., 2009). The emplacement age of the Fuchuan Ophiolite in the eastern segment of Jiangnan Orogenic Belt has also been revised to 850–820 Ma (SHRIMP and LA-ICP-MS zircon age) (Zhang et al., 2012, 2013), previously dated to 935 ± 10 Ma (mineral Sm—Nd isochron age) (Chen, 1991). The overlying Middle Neoproterozoic Banxi Group and contemporary sedimentary sequences were deposited in the intra-continental Nanhua rift basin during 800–715 Ma (Wang et al., 2015; Wang and Li, 2003). The Precambrian units, in turn, are overlain by lower Paleozoic marine and upper Paleozoic continental sequences, showing strong deformation related to intraplate orogenesis in the South China Block (Chu et al., 2012a, 2012b; Qiu et al., 2016; Yan et al., 2003).

The Dongling Complex is a NE-trending (30 km^2) body located at the southeastern margin of the Yangtze Block (Chen and Xing, 2016; Zhang et al., 2015a) (Fig. 2). It comprises phyllite, muscovite quartz schist, albite quartz schist, interlayered silicate and amphibolitic schist in the upper part, and biotite plagioclase gneiss, biotite K-feldspar gneiss and amphibolites in the lower part (BGMRAP, 1987), indicative of sedimentary and volcanic protolith (Zhang et al., 2015a). The Dongling Complex is intruded by the Cretaceous Hongzhen granite (Zhu et al., 2010). Regional extension and emplacement of Hongzhen granite have resulted in the uplift of the Dongling Complex from the middle crustal to the shallow crustal level (Grimmer et al., 2003; Zhu et al., 2010).

The Dongling granites are exposed in the Dongling area and also form the basement for the Quaternary sediments. The granites range from alkali feldspar granite to syenogranite and show evidence of minor deformation and low-grade metamorphism (Fig. 3a, b). The alkali feldspar granites comprise quartz (30–35%), K-feldspar (50–55%), minor plagioclase (~5%) and biotite (~5%), and accessory minerals (~2%), such as zircon and ilmenite (Fig. 3c, d). The syenogranites mainly comprise quartz (25–30%) and K-feldspar (50–55%), minor plagioclase (10%) and biotite (~2%) and accessory zircon and ilmenite (~2%) (Fig. 3e, f). Anhedral biotite occurs along the boundary between euhedral plagioclase and quartz (Fig. 3c-f), implying that the biotite is a later crystallizing phase. The Dongling granites show minor alteration, indicated by partial sericitization of feldspars.

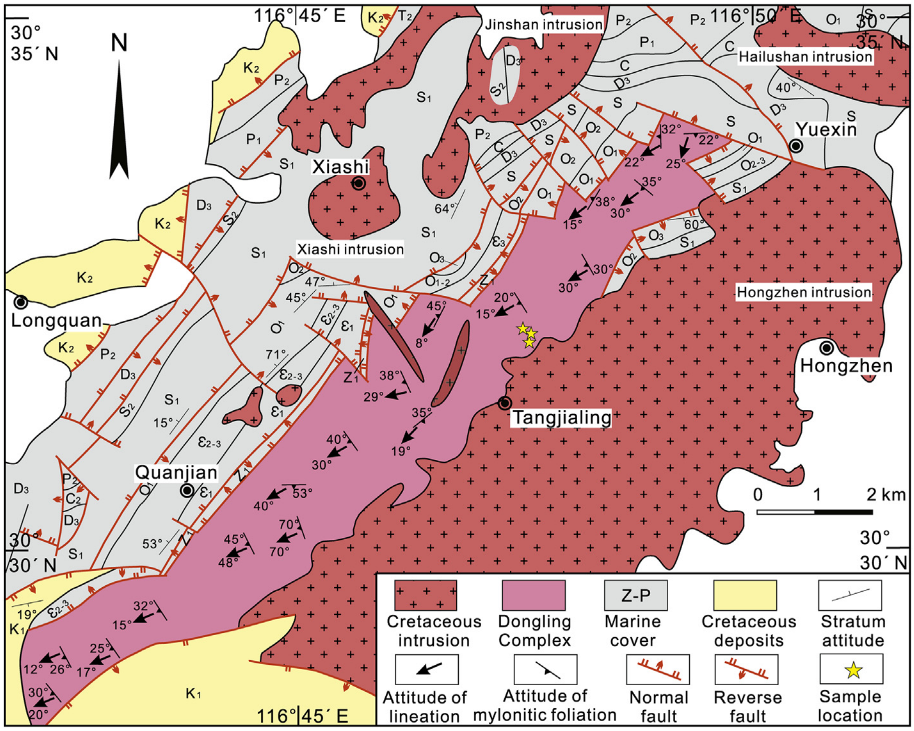

Fig. 2. Sketch geological map of the Dongling Complex (modified from Zhu et al. (2010), Zhang et al. (2015a) and Chen and Xing (2016)). The structural trends and data are from Zhu et al. (2010).

3. Analytical methods

3.1. Zircon U—Pb dating and Hf isotope analyses

Zircon grains were separated using standard heavy liquid and magnetic techniques, and handpicked using a binocular microscope. The separated zircons were mounted on epoxy resin and were polished to about half of their original size. Cathodoluminescence (CL) images of the zircons were taken using a Gatan Mono CL 3 attached to a JXA-8100 electron probe microanalyzer at the Guangzhou institute of Geochemistry, Chinese Academy of Sciences.

In-situ U—Pb isotope analyses of zircons were carried out using a Nu Instrument MC-ICP-MS, attached to a Resonetics Resolution M-50-HR excimer laser ablation system, at the University of Hong Kong. The laser beam diameter (with energy density of $5\ J\cdot cm^{-2}$ and 4 Hz repetition rate) was set at 30 μm. Helium was used as carrier gas to transport aerosol to the MC-ICP-MS system. Zircon 91,500 was used as the external standard to correct mass bias and element fraction, and GJ-1 was analyzed as the unknown sample to monitor the accuracy of the zircon age (Jackson et al., 2004). Raw data reduction was conducted off-line by software ICPMSDataCal program (Liu et al., 2010) and the results are reported with 1σ error. Common Pb was corrected following Andersen (2002). ISOPLOT software was used to calculated weighted zircon ages and depicted a Concordia plot (Ludwig, 2003). The concordant age of zircon GJ-1 is 598 ± 4 Ma ($n = 32$, MSWD = 0.13) (Supplementary Table 1), which coincides with the recommended age (GJ-1: 599.8 ± 1.7 Ma) (Jackson et al., 2004).

Lu—Hf isotope analyses were done using a Neptune Plus multi-collector (MC)-ICP-MS equipped with a 193 nm ArFexcimer laser ablation system, at the State Key Laboratory of Geological Process and Mineral Resources (SKLGPMR), China University of Geosciences, Wuhan. Diameter of the laser beam (with energy density of $15\ J\cdot cm^{-2}$ and pulse rate of 10 Hz) was set at 55 μm. Aerosol was transported to the ICP-MS system by helium, used as carrier gas. Details on laser ablation operating conditions and the MC-ICPMS instrument are provided in Li et al. (2010c). Protocol given in Liu et al. (2010) was followed for isobaric interference and instrumental mass bias corrections. Zircon 91,500 was used for quality control and zircon GJ-1 was analyzed as unknown sample to evaluate the accuracy of the analytical data. Raw data reduction was conducted off-line by software ICPMSDataCal program (Liu et al., 2010) and the results are reported with 1σ error. For calculation of $\varepsilon_{Hf}(t)$, T_{DM1}, T_{DM2} and $f_{Lu/Hf}$, the ^{176}Lu decay constant of 1.867×10^{-11} year^{-1}, $^{176}Hf/^{177}Hf_{CHUR} = 0.282772$, $^{176}Lu/^{177}Hf_{CHUR} = 0.0332$, $^{176}Hf/^{177}Hf_{DM} = 0.233251$ and $^{176}Lu/^{177}Hf_{DM} = 0.0384$ for the Chondritic Uniform Reservoir (CHUR) and Depleted Mantle (DM) were adopted (Blichert-Toft and Albarède, 1998; Griffin et al., 2002; Söderlund et al., 2004).

3.2. Whole-rock major and trace element analyses

Whole-rock major compositions were analyzed on fused glass beads using a Philips PW 2400 X-ray fluorescence spectrometer (XRF), at the University of Hong Kong. Trace element abundances were obtained using a Quadrupole ICP-MS, at the State Key Laboratory of Ore Deposit Geochemistry, Institute of Geochemistry, Chinese Academy of Sciences, Guiyang. One hundred milligrams sample powder each was digested with 0.5 ml of 68% HNO_3 (v/v) and 1 ml of 38% HF (v/v) in screw top PTFE-lined stainless steel bombs at 190 °C for 12 h. Closed beaker in high-pressure bombs was used to ensure complete dissolution. Insoluble residues were dissolved using 8 ml of 40% HNO_3 (v/v) heated to 100 °C for 3 h in an electric oven. All zircons were completely dissolved with nearly 100% recovery, therefore, this analytical procedure is particularly suitable for analyzing Zr and Hf. Detailed chemical separation and element measurement procedures are given in Qi et al. (2000). Pure elemental standards were used for external calibration and OU-1 and AMH-1 were used as reference materials. Accuracies of the XRF and ICP-MS analyses are better than 2% for major elements and 5% for most trace elements.

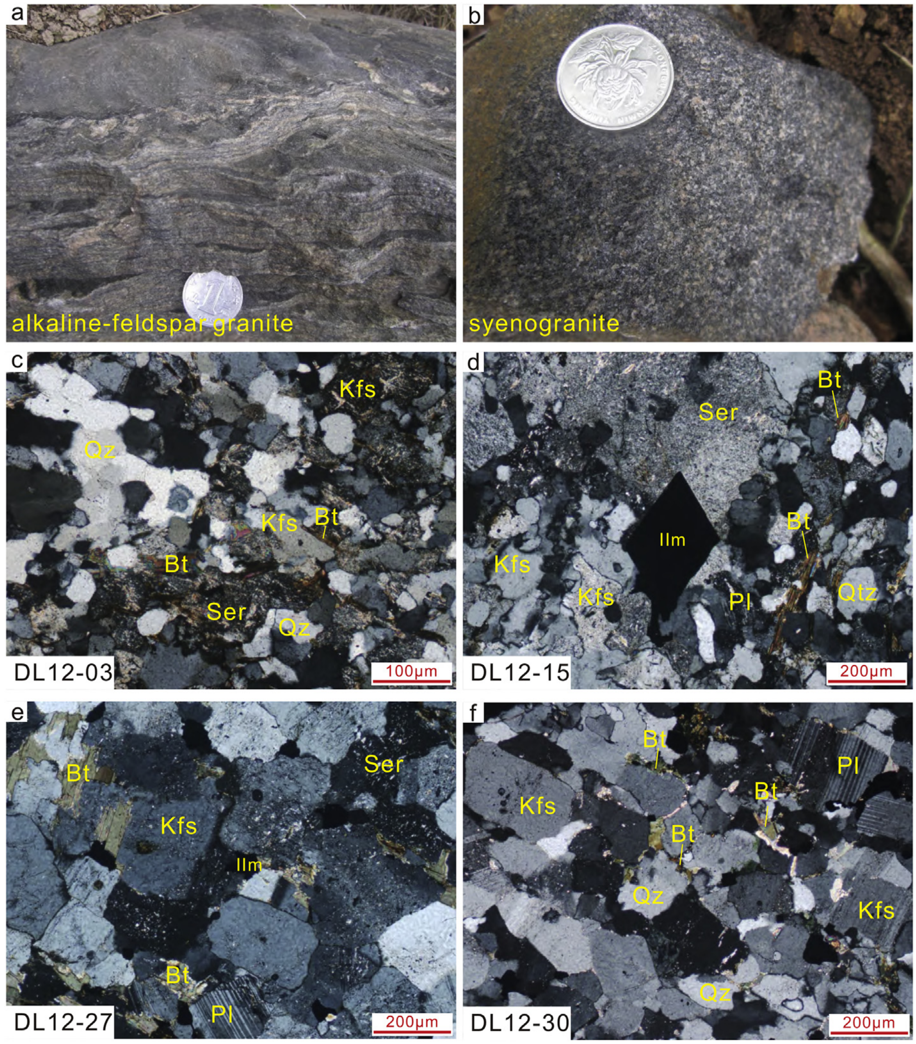

Fig. 3. Representative hand-specimen and thin section images of the Dongling granites. Abbreviations: Kfs: K-feldspar, Pl: Plagioclase, Qz: Quartz, Bt: Biotite, Ilm: Ilmenite, Ser: Sericite.

3.3. Whole-rock Rb—Sr and Sm—Nd isotopic determinations

Whole rock Rb—Sr and Sm—Nd isotopic analyses were carried out using a Multiple Collector Inductively Coupled Plasma Mass Spectrometer (MC-ICP-MS), at the Institute of Mineral Resource, Chinese Academy of Geological Sciences, Beijing, China. The sample powder was dissolved in distilled acetic acid for 24 h at 60 °C. The residues were further digested with HF + HNO_3 in Teflon capsules. The mixture was separated by conventional cation-exchange techniques. Strontium and Rare Earth Elements (REE) were separated and purified on quartz columns by conventional ion exchange chromatography with a 5-ml resin bed of AG 50 W-X12 (200–400 mesh) after sample decomposition. Nd and Sm were further separated from other REE on quartz columns using 1.7-ml Teflon powder coated with HDEHP, di(2-ethylhexy)orthophosphoric acid, as cation exchange medium. Further details on the analytical procedures are given in Chen et al. (2009). Measured $^{143}Nd/^{144}Nd$ and $^{87}Sr/^{86}Sr$ ratios were corrected for mass fractionation relative to reference values of $^{146}Nd/^{144}Nd = 0.7219$ and $^{87}Sr/^{86}Sr = 0.1194$, respectively. The results are reported in 2σ errors.

3.4. Electron Probe Micro Analyses (EPMA) of plagioclase and biotite

Compositions of plagioclase and biotite were determined at SKLGPMR, with a JEOL JXA-8100 Electron Probe Micro Analyzer equipped with four wavelength-dispersive spectrometers (WDS). Prior to analyses, the samples were coated with a ca. 20 nm conductive carbon film and the coated carbon way was suggested by Zhang and Yang (2016) to minimize the difference of carbon film thickness between sample and coating. The standards used for plagioclase were sanidine for K and Al, pyrope garnet for Fe, diopsode for Ca and Mg, jadeite for Na, rhodonite for Mn, rutile for Ti and olivine for Si. Additional standards used for biotite were fluorite for F, barite for Ba and almandine for Fe. Five μm and 10 μm spot sizes for plagioclase and biotite, respectively, with an accelerating voltage of 15 kV and a beam current of 20 nA working conditions were maintained during analyses. The peak and background counting time for majority of elements (Na, Mg, Al, Si, K, Ca, Fe and F) were 10 s and 5 s, respectively. For Ti and Mn, the double time relative to above elements peak and background counting time was used. On-line ZAF (atomic number, absorption, fluorescence) correction procedure was performed to calibrate the data.

4. Results

4.1. Zircon U—Pb ages and Hf isotopes

The CL images of representative zircons are shown in Fig. 4 and the results of LA-ICP-MS U—Pb and Lu—Hf isotopic analyses are presented in Supplementary Tables 2 and 3.

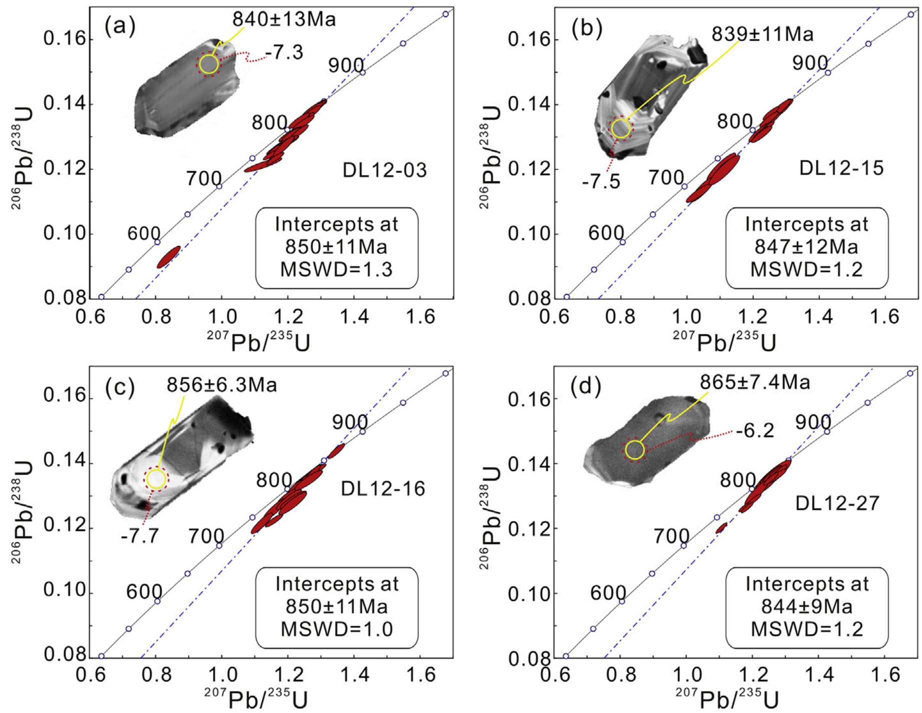

Fig. 4. LA-ICP-MS U—Pb zircon concordia diagrams for the Dongling granites (DL12–03, DL12–15, DL12–16 and DL12–27), South China. The inset diagram shows representative CL images; small yellow solid and large red dashed circles indicate areas of U—Pb and Lu—Hf isotope analyses, respectively. The corresponding ages and εHf(t) have also been indicated.

4.1.1. Alkali feldspar granite (DL12–03)

Zircon grains from this sample are 70–200 μm long, euhedral to subhedral in shape with length-width ratio between 1:1 and 1:3 (Fig. 4a). They have high Th/U ratios (0.47 to 1.35) (Supplementary Table 2) and exhibit oscillatory zoning or homogeneous internal structures. Majority of zircon grains show dark brown color in CL images, which is very likely due to high U and Th concentrations, implying a magmatic origin (Feng et al., 2014; Li et al., 2011). Some other granis appear colorless, probably due to later thermal overprint resulting in Pb loss. Thirty analyses were conducted on 26 zircon grains, in which eight analyses are not included in further calculation and discussion due to their discordant U—Pb ages or deviation from the major age group. In the concordia plot (Fig. 4a), the remaining 22 analyses define a discordia line with an upper intercept at 850 ± 11 Ma (MSWD = 1.3, n = 22), which is regarded as the crystallization age of the granite and is consistent with the weighted mean $^{207}Pb/^{206}Pb$ age of 843 ± 7 Ma (MSWD = 1.1, n = 22).

Magmatic zircons from this sample have initial $^{176}Hf/^{177}Hf$ ratio of 0.281989–0.282114 and $\varepsilon_{Hf}(t)$ values ranging from −8.8 to −4.4 with a weighted average $\varepsilon_{Hf}(t)$ value of −6.8 ± 0.8 (n = 12, MSWD = 2.7). These zircons have single-stage Hf isotopic model ages from 1.60 to 1.77 Ga while two-stage Hf isotopic model ages range from 2.01 to 2.29 Ga.

4.1.2. Alkali feldspar granite (DL12–15)

Zircon grains separated from alkali feldspar granite sample (DL12–15) are 50 to 200 μm long, euhedral to subhedral and have length-width ratio from 1.5:1 to 3:1 (Fig. 4b). Zircon grains show characteristic oscillatory zoning and have high Th/U ratios of 0.42 to 1.62 (Supplementary Table 2), indicative of an igneous origin. Seven of the thirty analyses are not included in the age calculation and subsequent discussion, due to their discordant U—Pb ages. In the concordia plot (Fig. 4b), remaining 23 analyses yield a discordia line that intersects the concordia curve at 847 ± 12 Ma (MSWD = 1.2, n = 23), which is consistent with the weighted mean $^{207}Pb/^{206}Pb$ age of 839 ± 6 Ma (MSWD = 0.76, n = 23) and is interpreted as the crystallization age of the rock.

Magmatic zircons from this sample have initial $^{176}Hf/^{177}Hf$ ratio of 0.281989–0.282078 and $\varepsilon_{Hf}(t)$ values ranging from −9.0 to −5.8 with a weighted average $\varepsilon_{Hf}(t)$ of −7.6 ± 0.6 (n = 12, MSWD = 1.4). The single-stage Hf isotopic model ages vary from 1.65 to 1.80 Ga and two-stage Hf isotopic model ages range from 2.10 to 2.29 Ga.

4.1.3. Alkali feldspar granite (DL12–16)

Zircon grains from this sample are 60 to 200 μm long, euhedral to subhedral in shape and length/width ratio ranging from 1:1 to 3:1 (Fig. 4c). These zircon grains show homogeneous internal structures with high Th/U ratios of 0.48 to 2.01, implying a magmatic origin (Supplementary Table 2). A single, out of the twenty five analyses is not included in the age calculation due to its discordant U—Pb age. In the concordia plot (Fig. 4c), the rest 24 analyses define a discordia line intersecting the concordia curve at 850 ± 11 Ma (MSWD = 1.0, n = 24), which is consistent with the weighted mean $^{207}Pb/^{206}Pb$ age of 851 ± 5 Ma (MSWD = 0.89, n = 24) and interpreted as the crystallization age of the rock.

Magmatic zircons from this sample (except #01 spot) have initial $^{176}Hf/^{177}Hf$ ratio from 0.281879 to 0.282085 and $\varepsilon_{Hf}(t)$ values varying from −12.8 to −5.5 with a weighted mean $\varepsilon_{Hf}(t)$ of −8.0 ± 0.6 (n = 11, MSWD = 2.1). The corresponding single-stage Hf isotopic model ages range from 1.63 to 1.95 Ga and two-stage Hf isotopic model ages from 2.08 to 2.53 Ga. The $\varepsilon_{Hf}(t)$ value of #01 spot is −21.9 and 3.09 Ga as the two-stage Hf isotope model age (Supplementary Table 3).

4.1.4. Syenogranite (DL12–27)

Zircon grains from syenogranite sample ((DL12–27) are 80 to 200 μm long, subhedral, colorless and have length-width ratio ranging from 2:1 to 3:1 (Fig. 4d). Most crystals show weak oscillatory zoning but high Th/U ratios (0.41 to 1.30) (Supplementary Table 2), indicating igneous origin. Two of twenty five analyses were discarded due to discordant U—Pb ages. Remaining 23 analyses define a discordia line

Table 1
Major element (in wt%) and trace element (in ppm) concentrations of the Dongling granites.

Sample	DL12–01	DL12–03	DL12–04	DL12–06	DL12–08	DL12–10	DL12–15	DL12–16	DL12–18	DL12–13	DL12–25	DL12–27	DL12–28	DL12–29	DL12–30	DL12–32
	Alkali feldspar granite									Syenogranite						
Major elements																
SiO_2	74.6	74.9	77.2	76.9	73.9	73.5	73.0	74.6	75.0	74.6	71.8	73.1	72.1	69.5	69.8	71.9
TiO_2	0.19	0.20	0.19	0.18	0.17	0.20	0.19	0.19	0.18	0.19	0.29	0.27	0.21	0.59	0.42	0.39
Al_2O_3	12.9	13.5	12.9	13.0	13.3	14.0	13.3	13.6	13.5	13.3	13.7	14.0	13.5	13.7	13.5	13.8
$Fe_2O_3^T$	2.02	2.10	1.18	0.63	1.94	1.87	2.37	2.08	2.05	2.35	2.81	2.43	2.46	4.88	4.45	3.61
MnO	0.03	0.05	0.02	0.01	0.05	0.03	0.04	0.03	0.06	0.08	0.07	0.06	0.07	0.07	0.09	0.05
MgO	0.20	0.18	0.07	0.13	0.19	0.18	0.14	0.14	0.13	0.15	0.34	0.26	0.27	0.54	0.29	0.26
CaO	0.30	0.28	0.21	0.21	0.16	0.25	0.41	0.40	0.21	0.71	1.21	0.89	0.97	1.02	1.10	0.90
Na_2O	2.00	1.87	2.85	2.89	2.12	1.94	2.65	2.37	2.05	3.31	4.15	3.40	4.18	4.05	3.90	3.44
K_2O	6.11	6.00	4.59	5.15	6.47	6.85	6.44	5.98	6.48	4.71	4.42	4.70	4.83	4.38	4.98	4.38
P_2O_5	0.04	0.03	0.03	0.03	0.03	0.04	0.02	0.03	0.03	0.03	0.05	0.04	0.03	0.15	0.07	0.06
LOI	1.19	1.13	0.99	0.81	0.99	1.20	0.67	0.68	0.63	0.52	0.62	0.59	0.75	0.75	0.72	0.65
TOTAL	99.6	100.2	100.2	99.8	99.3	100.0	99.2	100.1	100.3	99.9	99.4	99.7	99.4	99.6	99.3	99.4
A/NK[a]	1.30	1.41	1.34	1.25	1.26	1.32	1.17	1.32	1.30	1.26	1.18	1.31	1.11	1.20	1.14	1.33
A/CNK[b]	1.23	1.34	1.29	1.21	1.23	1.27	1.10	1.23	1.26	1.12	0.99	1.14	0.97	1.03	0.98	1.15
$Na_2O + K_2O$	8.11	7.87	7.44	8.04	8.59	8.79	9.09	8.35	8.53	8.02	8.57	8.09	9.01	8.43	8.87	7.82
$FeO^T/(FeO^T + MgO)$	0.90	0.91	0.93	0.94	0.90	0.91	0.94	0.93	0.82	0.93	0.88	0.89	0.89	0.89	0.93	0.93
Trace elements																
Li		12.2	3.99	1.01		6.47	12.9	4.74		7.44	15.90	5.70	5.39	7.59	5.04	3.99
Be		2.58	1.68	1.66		2.70	2.11	2.74		2.05	4.14	4.13	4.68	3.19	4.10	5.76
Sc		8.11	9.83	3.76		10.1	10.2	10.0		5.99	12.5	12.0	11.7	9.06	10.8	14.0
V		2.44	0.73	1.18		2.17	1.03	0.85		1.81	9.22	8.23	7.39	13.70	7.77	1.90
Cr		1.56	0.67	6.21		1.83	1.98	1.58		5.23	4.84	2.46	1.97	5.87	4.96	2.67
Co		0.76	0.54	0.56		1.08	0.65	0.43		0.87	2.56	1.39	1.37	2.45	1.95	0.83
Ni		0.14	0.14	2.45		0.84	0.27	0.12		2.45	2.57	0.84	0.65	2.65	3.00	0.53
Cu		30.6	4.32	7.79		3.00	8.25	2.89		8.30	7.30	2.31	1.77	7.15	9.60	3.12
Zn		313	19.2	60.5		120	96.5	76.4		137	151	73.6	69.5	114	79.9	88.3
Ga		21.7	17.7	12.7		20.6	21.0	22.6		18.0	24.0	22.5	21.9	20.9	23.0	25.1
Ge		0.96	0.81	0.78		0.91	0.90	1.05		0.88	1.30	1.28	1.26	1.22	1.69	1.31
As		0.13	0.14	1.93		0.10	0.12	0.11		4.12	2.44	0.12	0.11	2.42	1.84	0.16
Rb		134	102	127		170	155	169		137	145	141	139	130	132	112
Sr		75.9	52.9	41.9		65.6	63.4	65.2		68.3	104	88.8	93.0	93.8	155	73.1
Y		64.6	55.3	26.9		46.6	55.9	60.0		59.2	64.2	62.8	61.2	57.8	75.3	79.7
Zr		427	412	308		402	419	428		318	603	437	432	361	579	712
Nb		22.5	22.0	20.7		27.9	22.0	21.6		22.5	25.2	22.7	22.7	23.7	24.4	25.2
Sb		0.10	0.07	0.32		0.13	0.03	0.05		0.3	0.78	0.02	0.06	0.40	0.28	0.07
Cs		1.49	1.09	0.98		1.72	0.53	0.86		0.46	1.22	0.59	0.56	0.66	0.76	0.38
Ba		1009	995	1040		1044	1019	1017		885	1320	1017	1031	982	1540	1056
La		63.4	48.2	48.1		52.1	68.1	69.7		66.8	58.3	67.3	68.6	62.0	63.0	73.2
Ce		125	98.6	87.7		109	133	120		120	112	133	135	118	121	149
Pr		14.4	10.8	10.0		10.9	15.4	15.1		14.7	14.2	15.5	15.6	13.6	15.1	17.7
Nd		51.8	38.7	37.3		39.2	55.4	54.3		53.1	53.9	56.0	55.9	49.6	57.4	66.6
Sm		10.2	7.79	6.66		7.78	10.8	10.6		9.97	10.9	11.1	10.9	9.55	12.1	13.8
Eu		1.01	0.77	0.67		1.02	0.98	1.10		0.96	2.38	1.10	1.11	1.09	2.51	2.28
Gd		8.02	6.44	6.05		6.43	8.17	7.62		9.09	9.87	8.34	8.61	7.73	11.05	10.70
Tb		1.83	1.50	0.96		1.42	1.76	1.70		1.61	1.86	1.89	1.87	1.54	2.05	2.44
Dy		10.8	9.03	5.09		8.13	9.55	9.94		9.77	11.4	10.8	10.6	9.29	12.7	13.9
Ho		2.53	2.14	0.97		1.93	2.20	2.36		2.01	2.30	2.50	2.43	1.86	2.60	3.23
Er		7.04	6.07	2.87		5.27	6.19	6.92		6.38	7.18	6.96	6.76	5.85	8.15	8.95
Tm		1.04	0.92	0.38		0.76	0.92	1.06		0.93	1.11	1.03	1.00	0.87	1.23	1.31
Yb		6.68	6.07	2.41		5.05	6.05	7.07		5.94	7.48	6.76	6.70	5.75	8.05	8.56
Lu		0.99	0.90	0.34		0.73	0.91	1.07		0.91	1.08	1.01	0.99	0.87	1.19	1.28

(continued on next page)

Table 1 (*continued*)

Sample	DL12–01	DL12–03	DL12–04	DL12–06	DL12–08	DL12–10	DL12–15	DL12–16	DL12–18	DL12–13	DL12–25	DL12–27	DL12–28	DL12–29	DL12–30	DL12–32
	Alkali feldspar granite									Syenogranite						
Hf		12.1	11.8	9.19		11.4	12.1	12.4		9.08	13.8	12.3	12.4	9.5	13.6	17.9
Ta		1.37	1.41	1.09		2.24	1.26	1.19		1.13	1.45	1.42	1.46	1.54	1.50	1.50
W		1.32	1.01	1.18		1.81	0.44	0.52		1.53	1.92	0.73	1.01	1.01	1.31	0.84
Tl		1.13	0.66	0.78		1.33	1.11	1.31		0.86	1.28	0.81	0.79	0.80	0.81	0.57
Pb		210	18.9	10.3		91.1	65.5	35.7		36.1	27.3	23.6	24.0	24.6	20.9	25.3
Bi		0.12	0.05	0.61		0.12	0.02	0.03		0.25	1.12	0.08	0.08	0.36	0.94	0.02
Th		15.6	13.8	13.2		15.0	14.3	14.9		14.1	10.5	14.9	14.9	14.0	11.5	13.3
U		4.00	3.06	3.08		4.94	3.00	2.83		2.96	2.92	3.01	3.00	2.97	3.22	2.73
ΣREE		304	238	210		250	319	309		302	294	323	326	288	318	373
$(La/Yb)_N^c$		6.81	5.69	14.3		7.40	8.08	7.07		8.07	5.59	7.13	7.34	7.73	5.61	6.13
$(La/Sm)_N^c$		4.03	3.99	4.66		4.32	4.08	4.24		4.33	3.45	3.93	4.08	4.19	3.36	3.42
$(Gd/Yb)_N^c$		0.99	0.88	2.08		1.05	1.12	0.89		1.27	1.09	1.02	1.06	1.11	1.14	1.03
Eu/Eu*		0.34	0.33	0.32		0.44	0.32	0.37		0.31	0.70	0.35	0.35	0.39	0.66	0.57
10,000 × Ga/Al		3.0	2.6	1.9		2.8	3.0	3.1		2.6	3.3	3.0	3.1	2.9	3.2	3.4
Zr + Nb + Ce + Y		639	588	443		585	629	630		520	804	656	651	561	800	965
T_{Zr}^d		911	906	869		897	885	902		861	908	893	871	856	899	947

Note: [a]A/NK = $Al_2O_3/(Na_2O + K_2O)$; [b]A/CNK = $Al_2O_3/(CaO + Na_2O + K_2O)$; [c]Subscript *N* = chondrite-normalized value from Sun and McDonough (1989); [d]T_{Zr}: calculated by Zircon saturation thermometer of Watson and Harrison (1983).

with an upper intercept age of 844 ± 9 Ma (MSWD = 1.2, $n = 23$) (Fig. 4d), which is in close agreement with the weighted mean $^{207}Pb/^{206}Pb$ age of 846 ± 6 Ma (MSWD = 1.3, n = 23) and interpreted as the crystallization age of the rock.

Magmatic zircons from this sample have initial $^{176}Hf/^{177}Hf$ ratio ranging from 0.281935 to 0.282115 and $\varepsilon_{Hf}(t)$ values from −10.9 to −4.6 with a weighted average $\varepsilon_{Hf}(t)$ of −7.9 ± 1.1 ($n = 12$, MSWD = 5.8). The single-stage Hf isotopic model ages vary from 1.60 to 1.83 Ga and two-stage Hf isotopic model ages from 2.02 to 2.41 Ga.

4.2. Whole-rock major and trace elements

Sixteen samples were analyzed for whole rock major oxides and 13 samples for trace elements (Table 1). In the total alkali-silica (TAS) diagram all the samples classify as granite (Fig. 5a). In the Q′-ANOR diagram the samples can be discriminated into alkali feldspar granite and syenogranite (Fig. 5b), consistent with the modal mineral assemblages.

The Dongling alkali feldspar granites have high SiO_2 (73.0 to 77.2 wt%) and total alkalis ($K_2O + Na_2O$ = 7.44 to 9.09 wt%), low Al_2O_3 (12.9 to 14.0 wt%), $Fe_2O_3^T$ (0.63 to 2.37 wt%) and CaO (0.16 to 0.41 wt%) contents. The syenogranites have relatively lower SiO_2 (69.5 to 74.6 wt%), and higher Al_2O_3 (13.3 to 14.0 wt%), $Fe_2O_3^T$ (2.35 to 4.88 wt%) and CaO (0.71 to 1.21 wt%) contents but similar total alkali abundance ($K_2O + Na_2O$ = 7.82–9.01 wt%) as compared to the alkali feldspar granite. In the diagram of the A/CNK vs A/NK (Fig. 5c), the alkali feldspar granite are strongly peraluminous with high A/CNK values (1.10 to 1.34) while syenogranites have relatively lower A/CNK ratios (0.97 to 1.15). Moreover, these granites have high $FeO^T/(FeO^T + MgO)$ (0.82–0.94) and low P_2O_5 (0.02 to 0.15 wt%). In the Harker diagrams (Fig. 6), the SiO_2 shows inverse correlation with Al_2O_3, $Fe_2O_3^T$, TiO_2, P_2O_5, MgO, MnO, Sr, Zr and Ba, and covariance with Na_2O, K_2O and CaO.

The ΣREE concentrations for Dongling alkali feldspar granites and syenogranites range from 210 to 319 ppm and 288 to 373 ppm, respectively. The alkali feldspar granites are characterized by moderately to highly fractionated REE patterns ($(La/Yb)_N$ = 5.69–14.3) with flat heavy REE patterns ($(Gd/Yb)_N$ = 0.88–2.08) and remarkably negative Eu-anomalies (Eu/Eu* = 0.32 to 0.44) (Fig. 7a; Table 1). These granites are enriched in high field strength elements (HFSE) and large ion lithophile elements (LILE), such as Sr (41.9–75.9 ppm), Ba (995–1044 ppm), Zr (308–428 ppm), Nb (20.7–27.9 ppm), Y (26.9–64.6 ppm) and Zr + Nb + Ce + Y (443–639 ppm). The Dongling syenogranites exhibit similar REE patterns with $(La/Yb)_N$ values (5.59–8.07) and $(Gd/Yb)_N$ values (1.02–1.27) and moderately negative Eu anomalies (Eu/Eu* = 0.31 to 0.70) (Fig. 7a; Table 1) similar to the alkali feldspar granites. However, syenogranites have higher LILE (Sr = 68.3–155 ppm, Ba = 885–1540 ppm) and HFSE (Zr = 318–712 ppm, Nb = 22.5–25.2 ppm, Y = 59.2–79.7 ppm, Zr + Nb + Ce + Y = 520–965 ppm) concentrations as compared to alkali feldspar granite. In the primitive mantle normalized multi-element spider diagrams, all the samples define pronounced negative anomalies for Nb, Ta, Sr, Ti and slightly negative anomaly for Ba (Fig. 7b).

4.3. Whole-rock Rb—Sr and Sm—Nd isotopes

Eight Dongling granite samples were analyzed for whole rock Sr—Nd isotopic analyses and the data are presented in Table 2. Initial Sr—Nd isotopic compositions were calculated back to the emplacement ages of 850 Ma. The samples show a wide range of Rb/Sr (1.49–2.59) and $^{87}Sr/^{86}Sr_i$ ratios (0.677399 to 0.715292). Three samples (DL12–10, DL12–15 and DL12–16) have unrealistically low initial $^{87}Sr/^{86}Sr$ ratios (< 0.699), calculated by high $^{87}Rb/^{86}Sr$ ratios resulting from hydrothermal alteration, therefore, not discussed further. The analyzed samples have $^{147}Sm/^{144}Nd$ ratios from 0.1175 to 0.1253 and initial $^{143}Nd/^{144}Nd$ ratios from 0.510793 to 0.511104, corresponding to $\varepsilon_{Nd}(t)$ values of −14.6 to −8.6. Their single-stage model ages for Nd isotope range

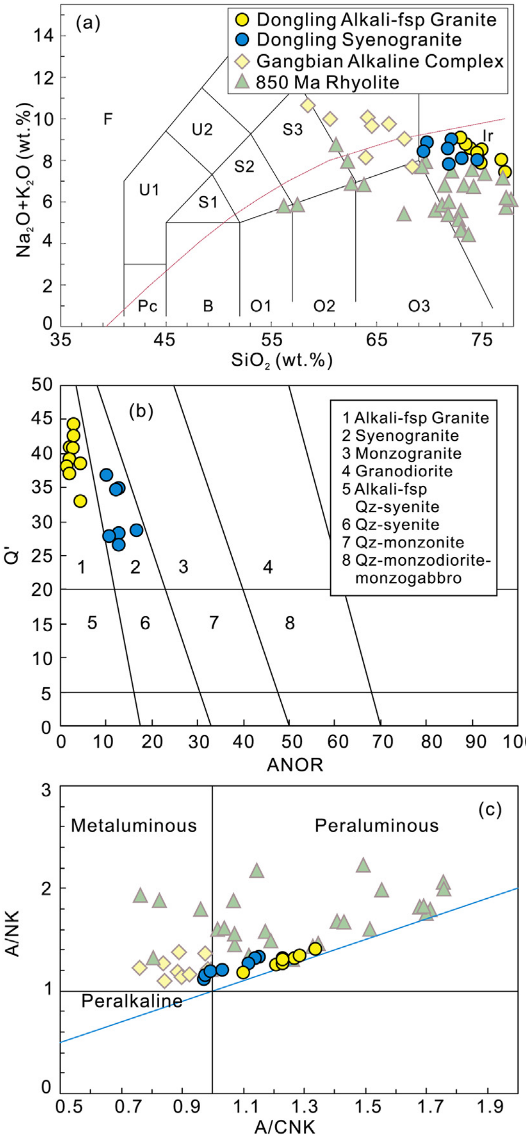

Fig. 5. (a) TAS classification diagram (after Middemost et al., 1994); (b) Q′-ANOR normative composition classification diagram (after Streckeisen and Maitre, 1979) of the Dongling granites, where $Q' = 100 \times Q/(Q + Or + Ab + An)$ and $ANOR = 100 \times An/(Or + An)$; (c) A/NK versus A/CNK diagram for the Dongling granites. $A/NK = Al/(Na + K)$ (molar ratio). $A/CNK = Al/(Ca + Na + K)$ (molar ratio). The Gangbian Alkaline Complex and 850 Ma rhyolite major and trace element data are from Li et al. (2010a, 2010b) and Lyu et al. (2017).

from 2.21 to 2.68 Ga and two-stage model ages from 2.20 to 2.69 Ga (Table 2).

4.4. Plagioclase and biotite mineral chemistry

A total of 43 spots on plagioclase grains of three syenogrnaite samples were analyzed by EPMA and the results are given in Table 3. The analyses show consistent SiO_2 (63.3–68.1 wt%), Al_2O_3 (19.7–21.6 wt%) and Na_2O (9.21–11.1 wt%) contents and lower and variable CaO (0.71–4.92 wt%), K_2O (0.10–1.45 wt%) and FeO^T (0.01–0.22 wt%) concentrations. Based on 8 oxygens in formula unit, the An content varies from 3.43 to 22.0 and Ab ranges from 74.4 to 96.0, characterizing Dongling syenogranite plagioclase as oligoclase-albite. Biotite data from Dongling alkali feldspar granite are presented in Table 4. Cations and related-parameters were calculated on 22 oxygens in formula unit of biotite and Fe^{2+} and Fe^{3+} values were obtained from Zheng (1983). Biotites have high FeO^T (25.5 to 29.4 wt%), consistent Al_2O_3 (17.1–19.0 wt%), SiO_2 (34.0–35.9 wt%) and moderate TiO_2 (2.29–4.10 wt%) contents (Table 4). High Ti^{4+} (0.27 to 0.48) and constant $Fe^{2+}/(Fe^{2+} + Mg^{2+})$ (0.81–0.84) of these biotites suggest unaltered chemical compositions, unaffected by any post-magmatic overprint (Table 4). Low MgO contents (2.39–2.82 wt%) and high FeO/(FeO + MgO) (0.91–0.92) (Table 4) values suggest that biotites are oxybiotite, specific type being sidero-phyllite.

5. Discussion

5.1. Effect of hydrothermal alteration on chemical compositions

The Dongling granites generally experienced slight but occasionally strong deformation and low-grade metamorphism, implying possible modification in geochemical signatures. Zr is considered as a highly immobile element and thus has been successfully employed as alteration-independent index of geochemical variations (Pearce and Peate, 1995; Polat et al., 2002). A positive correlation between Zr and TiO_2 further suggests insignificant modification and post-magmatic overprint on TiO_2 (Fig. 8a, except sample DL12–29). Therefore, TiO_2 could be employed as an alternative immobile element to evaluate the mobility of the major elements. In the present case, most elements, including LILE (K_2O, Na_2O, CaO, Sr and Ba), HFSE (Nb, Ta and Y) and REE (La, Ce, Nd, Sm and Yb) as well as some transition elements ($Fe_2O_3^T$), show well correlated relationship with TiO_2 and/or Zr, indicating their relative immobility during post-magmatic processes (Fig. 8b-h). Therefore, these immobile elements can be used to discuss and interpret the petrogenesis and geodynamic setting during the emplacement of the Dongling granites.

5.2. Emplacement age of the Dongling granites

The precise time for emplacement of the Dongling granites is loosely constrained prior to the present study. The Dongling Complex is traditionally considered as a counterpart of the Archean Kongling Complex in the northern Yangtze Block in spite of little reliable geochronological evidence. Whole rock Sm—Nd isochronal ages of 1895 ± 72 Ma (Xing et al., 1993) and 1439 ± 56 Ma (Dong and Qiu, 1993) for the plagioclase amphibole-schist have been considered as the robust evidence to regard the Dongling Complex as Paleoproterozoic terrane. This interpretation is broadly consistent with 1846 ± 20 Ma zircon mean $^{207}Pb/^{206}Pb$ protolith age for a drill core orthogenesis sample from the Dongling Complex (Chen and Xing, 2016). However, single zircon evaporation $^{207}Pb/^{206}Pb$ dating of a paragneiss in the Dongling Complex yielded three age populations, namely 2377–2370 Ma, 2016–1971 Ma and 783–692 Ma (Grimmer et al., 2003). These ages are in general agreement with the in-situ U—Pb detrital zircon ages from upper Dongling Complex with age clusters at > 2.4 Ga, ~2.0 Ga and 730–830 Ma (Zhang et al., 2015a). Therefore, the precise timing for the Dongling granites is still unclear and more data are needed.

In this study, zircons from the Dongling granites preserve oscillatory zoning and have high Th/U ratios (0.41–2.01), diagnostic of a magmatic zircon. Thus, the crystallization ages of 850 ± 11 Ma, 847 ± 12 Ma, 851 ± 5 Ma and 844 ± 9 Ma, are coherent and can be considered as the emplacement age of the Dongling granites. Although the 880–830 Ma was generally thought to be the period of magmatic quiescence in tectonics (Li et al., 2003, 2010b), abundant 860–840 Ma detritus, locally sourced, in sedimentary sequences younger than ~830 Ma in the Jiangnan Orogenic Belt indicate magmatic activity during this period (Sun et al., 2009; Wang et al., 2012, 2013; Zhao et al., 2011). More recent studies have identified significant magmatism within the Yangtze Block during this period, such as the 849 ± 7 Ma Shenwu dolerites (Li et al., 2008b), the 849 ± 6 Ma Zhenzhushan bimodal volcanic rocks (Li et al., 2010a), the 848 ± 4 Ma Gangbian Alkaline Complex (Li et al., 2010b), the 860 ± 9 Ma to 840 ± 5 Ma Huangshan and Meiling bimodal volcanic rocks

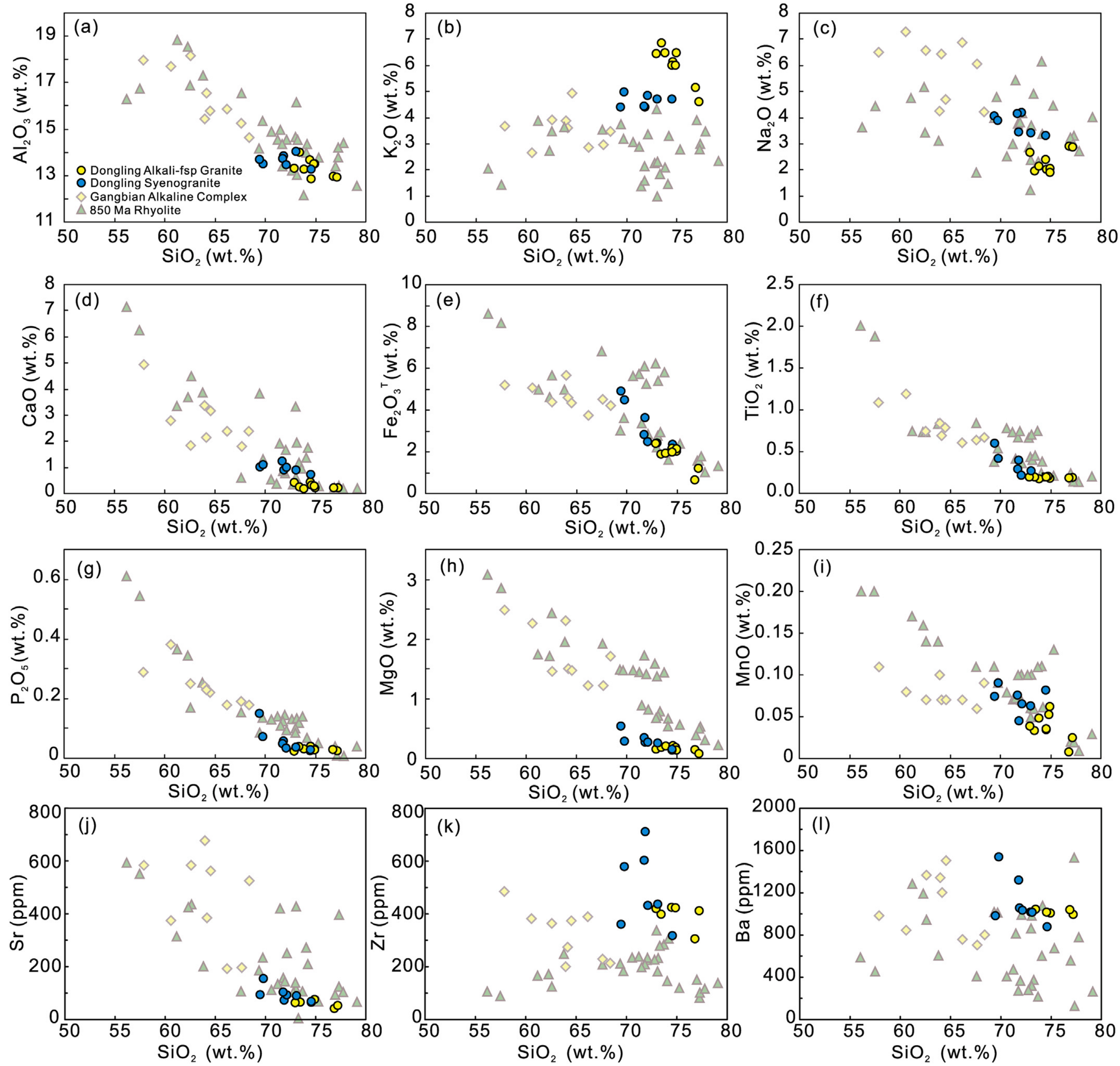

Fig. 6. Diagrams showing SiO_2 variation relative to major and trace elements in Dongling granites. The Gangbian Alkaline Complex and 850 Ma rhyolite major and trace element data are from Li et al. (2010a, 2010b) and Lyu et al. (2017).

(Lyu et al., 2017), the 852 ± 5 Ma strongly peraluminous granites (Wu et al., 2018) and some intermediate-basic magmatic rocks (Sun et al., 2017; Yao et al., 2014, 2015) (Fig. 1). All these data suggest that magmatism during 880–830 Ma was far more extensive than seen in present day limited exposures.

5.3. Temperature-pressure-water conditions of melting

Zircon saturation thermometry (T_{Zr}) can be used to estimate the initial temperature of the melting source, based on the zircon solubility, which is a function of temperature and magma composition (Miller et al., 2003; Watson and Harrison, 1983). The Dongling granites have calculated T_{Zr} of 856 to 947 °C (average 893 °C) (Table 1). This temperature may represent the minimum melt temperature because the Dongling granite magma was Zr under-saturated, as inferred from the absence of inherited and/or xenocrystic zircons. Therefore, the melting temperature must have been higher than 850 °C, similar to those of "hot granites" (Miller et al., 2003).

Ti content of biotite can serve as a geothermometer to evaluate its crystallization temperatures (Henry et al., 2005). Biotites from the Dongling granites have consistent X_{Mg} (0.13 to 0.16) and Ti^{4+} (0.27 to 0.48), corresponding to crystallization temperatures of 608 to 702 °C (average 660 °C) (Table 4), significantly lower than the zircon saturation temperatures. The textural relationships identify biotite as a late crystallizing phase (Fig. 2c-f), therefore, the biotite crystallization temperature represents a later stage temperature during the magma evolution.

High temperature-pressure experimental studies have established that anorthite (An) content of plagioclase as a function of temperature and H_2O content of the coexisting felsic melts (Dall'Agnol et al., 1999;

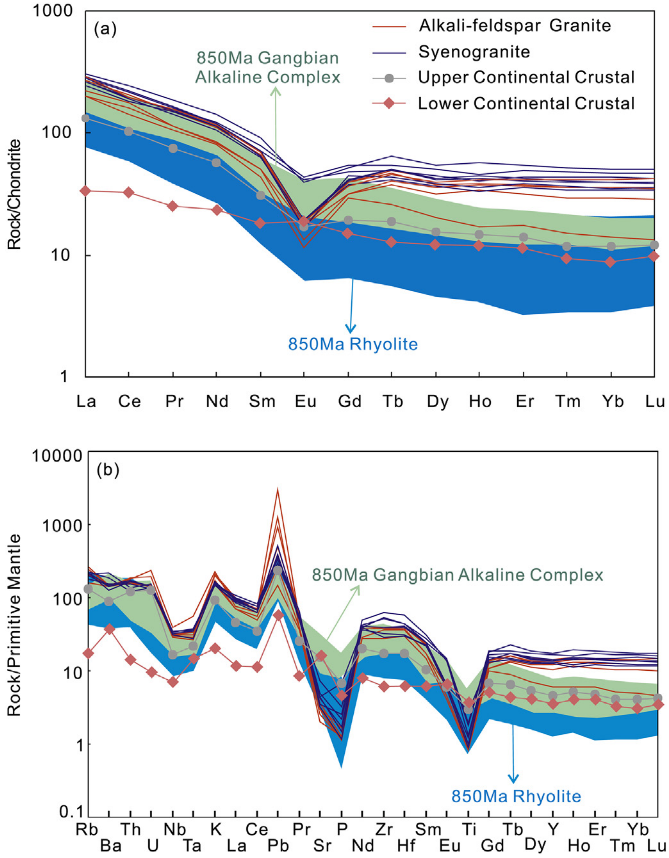

Fig. 7. (a) Chondrite-normalized REE diagram for Dongling granites. (b) Primitive mantle-normalized multi-element spider diagram for the Dongling granites. Chondrite and primitive mantle normalizing data are from Sun and McDonough (1989) and upper continental crust reference value is from Rudnick and Gao (2003). The Gangbian Alkaline Complex and 850 Ma rhyolite data are from Li et al. (2010a, 2010b) and Lyu et al. (2017).

Klimm et al., 2003). On the other hand, Klimm et al. (2008) argue that the mineral assemblage is controlled by major chemical composition and H_2O content of the melt. Based on An content (3.43–22.0: Table 3) and mineral assemblages, the least H_2O content of the Dongling granites has been estimated between 1.9 wt% and 2.6 wt% at 850 °C.

Uchida et al. (2007) summarized a pressure empirical equation, which can be used to estimate the solidification pressure of granitic rocks using total Al content of the biotite:

$$P\ (\text{MPa}) = \left(3.03 \times {}^{T}\text{Al}{-}6.53\ (\pm 0.33)\right) \times 100$$

where ^{T}Al designates the total Al in biotite. Biotite from the Dongling granites have ^{T}Al values ranging from 3.22 to 3.47 (Table 4), corresponding to a solidification pressure between 322 and 397 MPa (average 350 Mpa). Therefore, the pressure of the primary magma formed should be higher than 350 MPa. The granites have high Y (> 46 ppm, except sample DL12–06) and flat HREE patterns (Fig. 7a), indicating no garnet residue in the source region and partial melting at pressure lower than 700 MPa (Patiño Douce and Beard, 1996).

5.4. A-type granites and granulitic metasedimentary source

The Dongling granites have high $K_2O + Na_2O = (7.44–9.09$ wt%), ΣREE (210–373 ppm) and HFSE (Zr + Nb + Ce + Y = 443–965 ppm) contents as well as high 10,000 × Ga/Al ratios (> 2.6, except sample DL12–06), typical of A-type granites (Eby, 1992; Eby and Kochhar, 1990; Frost et al., 2001; Li et al., 2016; Whalen et al., 1987). Although

Table 2
Whole Rock Sr–Nd isotope compositions of the Dongling granites.

Sample	Lithology	Age (Ma)	Rb (ppm)	Sr (ppm)	$^{87}Rb/^{86}Sr$	$^{87}Sr/^{86}Sr$	±2σ	$^{87}Sr/^{86}Sr_i$	Sm (ppm)	Nd (ppm)	$^{147}Sm/^{144}Nd$	$^{143}Nd/^{144}Nd$	±2σ	$^{143}Nd/^{144}Nd(t)$	εNd(t)	T_{DM1} (Ga)	T^{a}_{DM2} (Ga)	$f_{Sm/Nd}$
DL12–03	Alkali feldspar granite	850	134	75.9	5.010	0.769527	14	0.708686	10.2	51.8	0.1186	0.511765	18	0.511104	−8.6	2.21	2.20	−0.40
DL12–04		850	102	52.9	5.468	0.767609	9	0.701205	7.79	38.7	0.1218	0.511699	23	0.511020	−10.2	2.39	2.33	−0.38
DL12–10		850	170	65.6	7.339	0.766520	7	0.677399	7.78	39.2	0.1200	0.511671	11	0.511001	−10.6	2.40	2.36	−0.39
DL12–15		850	155	63.4	6.940	0.766521	9	0.682243	10.8	55.4	0.1175	0.511448	21	0.510793	−14.6	2.68	2.69	−0.40
DL12–16		850	169	65.2	7.341	0.766672	5	0.677526	10.6	54.3	0.1180	0.511665	8	0.511007	−10.5	2.36	2.36	−0.40
DL12–27	Syeno-granite	850	141	88.8	4.510	0.766851	8	0.712080	11.1	56.0	0.1195	0.511658	5	0.510992	−10.7	2.40	2.38	−0.39
DL12–28		850	139	93.0	4.237	0.766745	11	0.715292	10.9	55.9	0.1176	0.511665	7	0.511009	−10.4	2.35	2.35	−0.40
DL12–32		850	112	73.1	4.358	0.766766	9	0.713841	13.8	66.6	0.1253	0.511746	12	0.511048	−9.7	2.41	2.29	−0.36

Note: $^{a}T_{DM2} = T_{DM1} - (T_{DM1} - \text{rocks age}) \times (-0.4 - (^{147}Sm/^{144}Nd/0.1967 - 1)/(-0.4 - 0.08592)$

Table 3
Chemical compositions (wt%) of plagioclase from the Dongling syenogranite.

Spot.	SiO_2	TiO_2	Al_2O_3	FeO^T	MnO	MgO	CaO	Na_2O	K_2O	Total	An	Ab	Or
DL12–28-01	67.6	–	20.8	0.10	0.01	–	1.91	10.9	0.16	101.4	8.78	90.4	0.9
DL12–28-02	65.2	0.01	21.4	0.10	0.02	0.05	2.68	9.67	0.63	99.7	12.8	83.6	3.6
DL12–28-03	66.7	–	20.6	0.07	–	–	1.63	10.7	0.12	99.8	7.73	91.6	0.7
DL12–28-04	67.1	0.03	21.1	0.08	0.00	–	2.14	10.3	0.28	101.0	10.2	88.3	1.6
DL12–28-05	67.7	–	20.6	0.11	–	0.03	1.58	10.0	0.21	100.2	7.94	90.8	1.3
DL12–28-06	66.7	0.02	21.0	0.12	0.00	0.02	2.06	10.6	0.37	100.8	9.51	88.5	2.0
DL12–28-07	66.8	–	20.9	0.17	–	0.02	2.06	10.4	0.38	100.8	9.64	88.3	2.1
DL12–28-08	67.8	–	20.6	0.08	–	–	1.27	10.9	0.15	100.9	5.97	93.2	0.9
DL12–28-09	66.8	–	20.5	0.01	–	0.00	1.63	10.4	0.36	99.7	7.79	90.1	2.1
DL12–28-10	66.7	–	20.8	0.15	0.00	–	1.90	10.6	0.41	100.6	8.79	88.9	2.3
DL12–28-11	66.2	–	20.7	0.09	–	–	2.09	10.2	0.28	99.5	10.0	88.4	1.6
DL12–28-12	66.5	–	20.7	0.13	–	–	1.98	10.2	0.40	99.9	9.47	88.3	2.3
DL12–28-13	67.0	0.00	20.7	0.10	–	0.02	1.83	10.4	0.35	100.3	8.69	89.3	2.0
DL12–28-14	67.1	–	20.8	0.03	0.03	–	1.94	10.4	0.34	100.6	9.21	88.9	1.9
DL12–28-15	67.0	–	20.7	0.07	–	–	1.96	10.4	0.31	100.5	9.26	89.0	1.8
DL12–27-01	67.1	–	20.9	0.11	0.01	–	2.31	10.2	0.30	101.0	10.9	87.4	1.7
DL12–27-02	67.1	–	21.1	0.08	0.08	0.02	2.03	10.2	0.34	100.8	9.75	88.3	1.9
DL12–27-03	67.6	–	20.6	0.10	0.01	–	1.79	10.4	0.39	100.9	8.47	89.3	2.2
DL12–27-04	67.3	–	21.0	0.11	–	0.00	2.12	10.0	0.47	101.0	10.2	87.1	2.7
DL12–27-05	67.5	–	20.6	0.12	0.01	0.00	1.90	10.2	0.33	100.7	9.17	88.9	1.9
DL12–27-06	67.1	–	20.8	0.15	0.02	–	2.01	10.2	0.40	100.7	9.59	88.1	2.3
DL12–27-07	66.5	–	20.6	0.09	0.01	0.01	1.93	10.3	0.30	99.7	9.25	89.0	1.7
DL12–27-08	66.4	0.02	20.8	0.10	0.01	0.01	2.11	10.6	0.26	100.3	9.78	88.8	1.4
DL12–27-09	68.1	0.01	19.7	0.21	0.00	0.00	0.71	11.1	0.10	99.9	3.43	96.0	0.6
DL12–27-10	67.2	0.01	20.5	0.09	0.00	–	1.60	10.7	0.24	100.4	7.51	91.2	1.3
DL12–27-11	64.4	0.00	21.5	0.15	0.02	0.05	2.55	9.47	1.45	99.6	11.9	80.0	8.1
DL12–27-12	67.4	0.01	21.3	0.22	–	0.02	1.16	10.2	0.85	101.2	5.63	89.5	4.9
DL12–27-13	67.1	–	20.8	0.16	0.03	0.05	1.52	10.1	0.51	100.4	7.43	89.6	3.0
DL12–27-14	66.3	–	20.6	0.13	–	–	2.11	10.2	0.38	99.8	10.0	87.8	2.2
DL12–27-15	65.8	–	21.1	0.07	–	–	2.17	10.2	0.29	99.7	10.3	88.1	1.6
DL12–27-16	65.5	–	21.6	0.11	0.01	–	2.02	9.83	0.49	99.6	9.89	87.3	2.9
DL12–27-17	66.9	–	20.8	0.12	0.02	0.01	1.91	10.4	0.31	100.5	9.02	89.2	1.8
DL12–27-18	67.4	–	20.7	0.13	0.02	0.03	1.91	10.4	0.47	101.1	8.99	88.4	2.6
DL12–30-01	65.6	0.01	21.3	0.13	–	0.00	2.77	10.1	0.35	100.3	12.9	85.1	1.9
DL12–30-02	66.6	–	21.3	0.09	0.00	–	2.44	10.4	0.14	100.9	11.4	87.8	0.8
DL12–30-03	66.1	–	21.5	0.17	0.01	0.01	2.47	10.0	0.14	100.4	11.9	87.3	0.8
DL12–30-04	66.6	–	21.4	0.26	–	–	2.47	10.3	0.27	101.2	11.5	87.0	1.5
DL12–30-05	66.5	–	20.8	0.11	0.01	–	2.22	10.6	0.10	100.3	10.3	89.1	0.6
DL12–30-06	66.4	–	21.2	0.11	–	–	2.42	10.4	0.20	100.7	11.3	87.6	1.1
DL12–30-07	63.3	0.02	20.5	0.07	0.03	0.04	4.92	9.21	0.69	98.8	22.0	74.4	3.7
DL12–30-08	66.8	0.01	20.0	–	–	–	2.52	10.7	0.16	100.3	11.4	87.7	0.9
DL12–30-09	67.1	0.01	21.3	0.12	–	–	1.96	10.1	0.39	101.0	9.43	88.4	2.2
DL12–30-10	66.6	–	21.1	0.09	0.00	0.02	2.08	10.2	0.36	100.5	9.93	88.0	2.0

the Dongling granites have high A/CNK values (0.97–1.34), their A-type affinity is further supported by rather low P_2O_5 contents (0.02 to 0.15 wt%) and no phosphate observation in the sections (Bonin, 2007; King et al., 1997). In the discriminating plots (Fig. 9a-d), the Dongling granite samples are plotted in the A-type granite fields. These granites are ferroan alkali-calcic to alkaline in composition and have high $FeO^T/(FeO^T + MgO)$ (0.82–0.94) and moderate $Na_2O + K_2O$ – CaO (6.92–8.68 wt%) (Fig. 9e, f). The A-type affinity of the Dongling granites is also in agreement with the estimated high melting temperature (higher than 850 °C) and thus can be regarded as the first identified ~850 Ma A-type felsic pluton in the Yangtze Block, South China.

The A-type granites are chemically variable and could be formed from diverse source rocks and petrogenetic processes (Bonin, 2007). Proposed models include (1) fractionation of mantle-derived alkaline basaltic or tholeiitic magmas (Frost et al., 1999; Frost and Frost, 1997; Turner et al., 1992); (2) partial melting of granulitic crustal residues after extraction of early granite magmas (Anderson and Thomas, 1985; Bea and Montero, 1999; Clemens et al., 1986; Collins et al., 1982; Creaser et al., 1991; Whalen et al., 1987); (3) low pressure melting of calc-alkaline rocks at upper crustal levels (Patiño Douce, 1997; Skjerlie and Johnston, 1992) and (4) integrated crustal- and mantle-derived materials, either crustal assimilation and fractional crystallization of mantle-derived magmas, or hybridization between mantle-derived melts and anatectic granitic magmas (Griffin et al., 2002; Kemp et al., 2005; Yang et al., 2006).

The Dongling granites have remarkably negative zircon $\varepsilon_{Hf}(t)$ (-12.8 to -4.6) and whole rock $\varepsilon_{Nd}(t)$ (-14.6 to -8.6), which are significantly lower than the coeval intermediate-mafic juvenile crust (Fig. 10), ruling out the possibility of the granites being differentiation products of mantle-derived magmas and suggesting a mature crustal source. Chemical characteristics of biotite also suggest a crustal origin for the Dongling granites, ruling out any crust-mantle maxing (Fig. 11). This interpretation is also supported by the absence of mafic enclaves and acicular apatite as well as no bimodal distribution of zircon $\varepsilon_{Hf}(t)$ and whole rock $\varepsilon_{Nd}(t)$ values representing magma mixing. In the $\varepsilon_{Nd}(t)$ vs $^{87}Sr/^{86}Sr_i$ diagram (Fig. 12), the samples plot in the mature continental crustal field, substantiating derivation from partial melts of ancienct continental crustal. Therefore, we interpret a mature continental crustal source for the Dongling granites without any notable mantle input.

At higher crustal levels, high temperature melting of tonalite and granodiorite can potentially generate metaluminous A-type magmas (Patiño Douce, 1997; Skjerlie and Johnston, 1992). The Dongling granites are weakly to strongly peraluminous (A/CNK = 0.97 to 1.34) (Fig. 5c), and formed under > 350 to < 700 MPa pressure, inconsistent with their derivation from calc-alkaline felsic igneous rocks in the upper crust. The zircon saturation thermometry suggests melting at temperatures above 850 °C. Such high temperatures can be realized in

Table 4
Chemical compositions (wt%) of biotite from the Dongling alkali feldspar granite (DL12–16).

Spot.	1	2	3	4	5	6	7	8	9	10	11	12	13	14	15	16	17	18	19	20
SiO_2	35.9	34.4	34.6	34.8	34.4	34.4	34.4	33.7	34.4	34.7	35.1	34.7	34.0	34.6	34.5	34.8	34.6	34.6	34.5	34.7
TiO_2	2.65	2.85	2.84	3.27	2.29	3.51	2.91	3.36	3.27	3.31	3.62	3.55	3.02	2.90	2.60	3.10	4.10	3.49	3.15	3.08
Al_2O_3	19.0	18.3	17.3	18.2	17.3	17.8	17.8	17.8	17.5	17.6	17.9	18.4	17.1	18.3	17.8	17.9	17.5	17.5	18.2	18.0
FeO^T	25.5	27.7	28.7	27.0	29.4	27.9	27.5	28.1	28.0	27.8	27.2	26.5	28.3	27.2	28.0	27.2	27.2	27.7	27.6	27.5
MnO	0.32	0.34	0.30	0.29	0.33	0.30	0.31	0.32	0.32	0.34	0.26	0.30	0.29	0.30	0.36	0.31	0.26	0.29	0.29	0.31
MgO	2.48	2.50	2.53	2.68	2.77	2.63	2.40	2.63	2.59	2.49	2.82	2.39	2.56	2.63	2.63	2.60	2.43	2.54	2.48	2.59
Na_2O	0.12	0.19	0.11	0.14	0.09	0.12	0.29	0.12	0.14	0.21	0.21	0.21	0.24	0.26	0.23	0.21	0.24	0.18	0.14	0.19
K_2O	9.41	9.62	9.60	9.66	9.22	9.57	9.47	9.63	9.47	9.47	9.44	9.52	9.35	9.35	9.52	9.74	9.58	9.47	9.72	9.57
F	0.72	0.75	0.73	0.65	0.66	0.49	0.84	1.08	0.67	0.73	0.05	0.52	0.49	0.62	0.80	1.13	0.54	0.98	0.80	0.65
Total	95.9	96.4	96.6	96.5	96.2	96.6	95.5	96.3	96.1	96.2	96.6	95.9	95.2	95.9	96.1	96.6	96.2	96.3	96.7	96.3
Cations based on 22 oxygens																				
Si	5.57	5.40	5.46	5.43	5.45	5.40	5.44	5.32	5.43	5.45	5.48	5.44	5.44	5.44	5.44	5.43	5.43	5.42	5.40	5.44
Al^{IV}	2.43	2.60	2.54	2.57	2.55	2.60	2.56	2.68	2.57	2.55	2.52	2.56	2.56	2.56	2.56	2.57	2.57	2.58	2.60	2.56
T-site	8.00	8.00	8.00	8.00	8.00	8.00	8.00	8.00	8.00	8.00	8.00	8.00	8.00	8.00	8.00	8.00	8.00	8.00	8.00	8.00
Al^{VI}	1.03	0.78	0.67	0.79	0.68	0.70	0.76	0.61	0.69	0.70	0.78	0.84	0.67	0.82	0.74	0.72	0.67	0.66	0.76	0.77
Ti^{4+}	0.31	0.34	0.34	0.38	0.27	0.41	0.35	0.40	0.39	0.39	0.43	0.42	0.36	0.34	0.31	0.36	0.48	0.41	0.37	0.36
Fe^{3+}	0.84	0.62	0.60	0.67	0.55	0.61	0.65	0.65	0.64	0.67	0.60	0.71	0.55	0.65	0.61	0.71	0.67	0.72	0.66	0.64
Fe^{2+}	2.47	3.01	3.19	2.86	3.35	3.05	2.98	3.06	3.05	2.98	2.96	2.76	3.24	2.93	3.08	2.84	2.90	2.91	2.96	2.97
Mn	0.04	0.05	0.04	0.04	0.04	0.04	0.04	0.04	0.04	0.05	0.03	0.04	0.04	0.04	0.05	0.04	0.03	0.04	0.04	0.04
Mg	0.57	0.59	0.59	0.62	0.65	0.62	0.57	0.62	0.61	0.58	0.66	0.56	0.61	0.62	0.62	0.61	0.57	0.59	0.58	0.61
B-site	5.27	5.39	5.43	5.36	5.55	5.43	5.34	5.38	5.42	5.37	5.45	5.33	5.47	5.40	5.41	5.28	5.33	5.33	5.36	5.39
Ca	0.00	0.00	0.00	0.00	0.00	0.00	0.00	0.00	0.00	0.00	0.01	0.00	0.00	0.00	0.00	0.00	0.00	0.00	0.00	0.00
Na	0.04	0.06	0.03	0.04	0.03	0.04	0.09	0.04	0.04	0.06	0.06	0.06	0.07	0.08	0.07	0.06	0.07	0.06	0.04	0.06
K	1.86	1.93	1.93	1.92	1.86	1.92	1.91	1.94	1.91	1.90	1.88	1.90	1.91	1.87	1.91	1.94	1.92	1.89	1.94	1.92
A-site	1.90	1.99	1.97	1.96	1.89	1.95	2.00	1.97	1.95	1.96	1.95	1.97	1.98	1.96	1.98	2.00	2.00	1.95	1.98	1.97
^{T}Al	3.47	3.38	3.22	3.36	3.23	3.30	3.32	3.30	3.26	3.25	3.30	3.40	3.23	3.38	3.30	3.29	3.25	3.24	3.36	3.33
$Fe^{2+}/(Fe^{2+}+Mg^{2+})$	0.81	0.84	0.84	0.82	0.84	0.83	0.84	0.83	0.83	0.84	0.82	0.83	0.84	0.83	0.83	0.82	0.84	0.83	0.84	0.83
Mg/(Mg + Fe)	0.15	0.14	0.14	0.15	0.14	0.14	0.13	0.14	0.14	0.14	0.16	0.14	0.14	0.15	0.14	0.15	0.14	0.14	0.14	0.14
FeO/(FeO + MgO)	0.91	0.92	0.92	0.91	0.91	0.91	0.92	0.91	0.92	0.92	0.91	0.92	0.92	0.91	0.91	0.91	0.92	0.92	0.92	0.91
P(MPa)[a]	397	372	322	365	325	347	353	346	335	332	345	378	325	371	348	345	331	328	366	356
T(°C)[b]	631	646	646	667	608	679	650	673	669	670	683	680	658	648	631	658	702	678	661	658

Note: [a]P (MPa) = $(3.03 \times {}^{T}Al - 6.53\,(\pm 0.33)) \times 100$, where ^{T}Al designates the total Al in biotite on the basis of O = 22; [b]$T = \{[\ln(Ti^{4+}) - a - c \times X_{Mg}^3]/b\}^{0.333}$, $a = -2.3594$, $b = 4.6482 \times 10^{-9}$, $c = -1.7283$, $X_{Mg} = Mg/(Mg + Fe)$.

the deeper crust (Clemens, 1990 and references there in), further rule out an upper crustal origin.

Alternatively, A-type granites can be generated by high temperature melting of granulitic metasedimentary/metaigneous residues after early granitic melt extraction (Anderson and Thomas, 1985; Clemens et al., 1986; Collins et al., 1982). Experiments have revealed that refractory granulitic residues, after partial melting of a wide range of crustal rocks, are depleted in total alkalis and TiO_2 relative to Al_2O_3 and MgO, respectively (Patiño Douce and Beard, 1995, 1996). The Dongling granites have low $(Na_2O + K_2O)/Al_2O_3$ (0.56–0.68) and TiO_2/MgO (0.78–2.64) ratios, indicating that these granites were derived from a granulitic residues. However, Creaser et al. (1991) have suggested that the residual source remaining after generation of I-type granite is unlikely to generate a partial melt with the appropriate major element characteristics of A-type granites. Experimental studies on granitic melts indicate that pelite-derived granites tend to have lower CaO/Na_2O ratios (< 0.3) than psammite/igneous-derived counterparts (Jung and Pfander, 2007; Sylvester, 1998). The Dongling granites have CaO/Na_2O ratios ranging from 0.07 to 0.29 (Table 1), similar to those of pelite-derived granites (Jung and Pfander, 2007). Some Proterozoic granulitic metapelitic rocks have been reported in the northern Yangtze Block (Sun et al., 2008). Metasedimentary rocks may contain appropriate minerals and geochemical compositions required for A-type magmatism, as evidenced from the Ivrea zone of the south Alps where granulite facies metapelites (stronalites) contain quartz, K-feldspar, plagioclase, and subordinate biotite (Bea and Montero, 1999). In addition, the Dongling granites also have variable two-stage Nd and Hf model ages (2.01–2.69 Ga), indicating a heterogeneous source region similar to sedimentary rocks. Therefore, the 850 Ma Dongling granites were derived from a granulitic metasedimentary source.

5.5. Geodynamic setting of the Dongling A-type granites and its implications on the early Neoproterozoic tectonic evolution of the South China Block

The A-type granites were considered to have generated in anorogenic or within plate settings (Collins et al., 1982; Dong et al., 2011; Eby, 1990, 1992; Turner et al., 1992; Whalen et al., 1987; Zhao et al., 2008, 2018), however, recent studies also suggest their emplacement in localized extension within an active convergent margin, such as the back-arc extensional environment (Hu et al., 2018; Li et al., 2016; Liu et al., 2018; Wang et al., 2018b). Although the A-type classification is not source specific, Eby (1990, 1992) proposed their discrimination into A1- and A2- type, depending upon their source characteristics. The A1-type granites represent differentiates of magmas derived from sources like oceanic-island basalts, thus generated under intraplate setting. In contrast, the A2-type granites represent magmas derived from continental crustal or underplated crust that has been through a cycle of continent-continent collision or island-arc magmatism, and are attributed to continental crust at convergent margins. The Dongling granites have high Y/Nb (1.3–3.1) and Ce/Nb (3.9–6.1) ratios, resembling A-type magmas derived from sources chemically similar to continental margin basalts rather than oceanic-island basalts (Eby, 1992; Fig. 13a), which is also evidenced by their high Yb/Ta (2.2–5.9) ratios. The Y/Nb-Sc/Nb, Nb-Y-Ce and Nb-Y-3Ga plots clearly underline A2-type affinity for the Dongling granites (Fig. 13b, c). All the above discussed geochemical parameters underline emplacement of the Dongling A-type granites in a post-collision extensional environment in a convergent continental margin.

The extensional setting at ca. 850 Ma is also supported by several volcanic and intrusive rocks exposed along the southeastern margin of the Yangtze Block, such as the Shenwu dolerites, the strongly

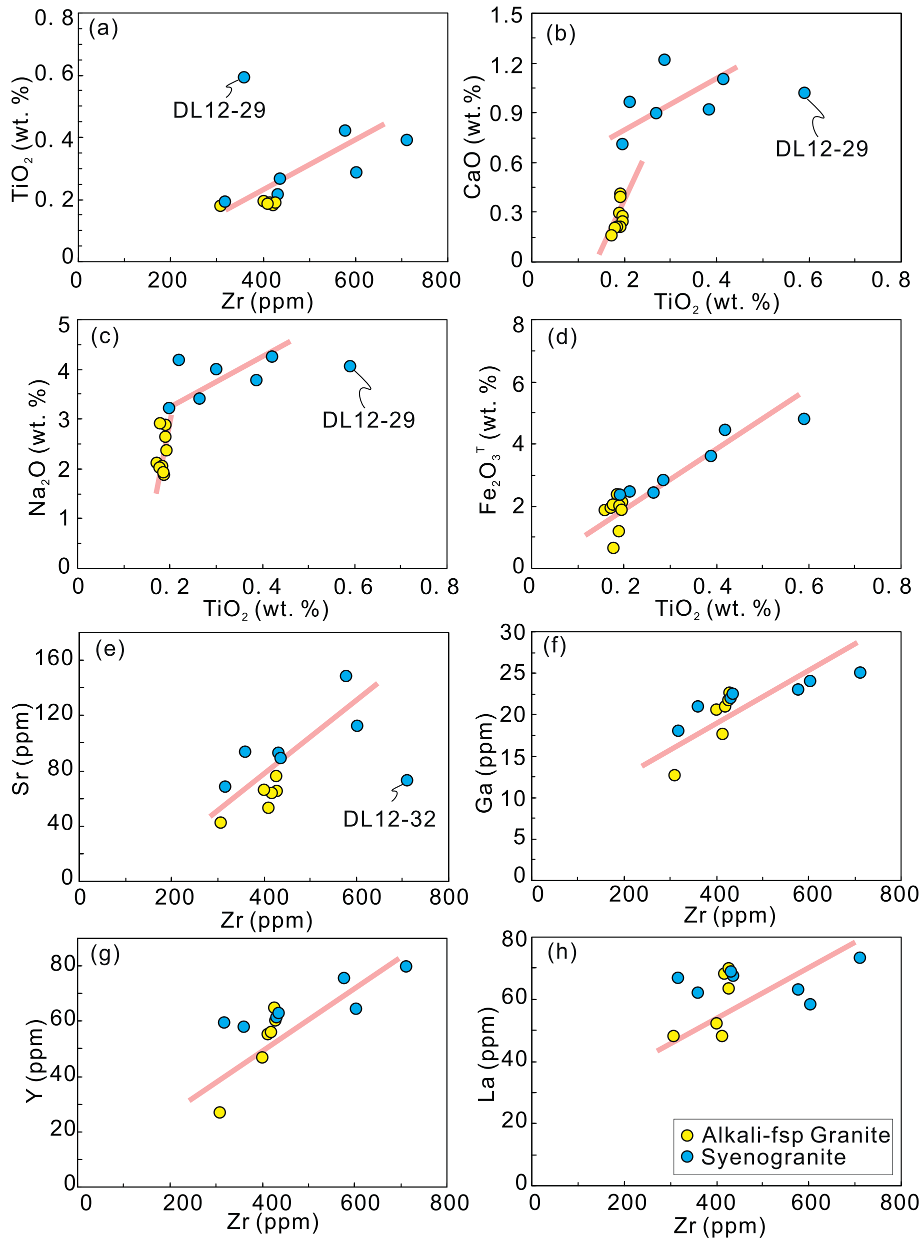

Fig. 8. Bi-elemental plots of the TiO_2 and Zr versus CaO, Na_2O, $Fe_2O_3^T$, Sr, Ga, Y and La to evaluate the mobility of these elements (including LILE, REE and HFSE) in studied Dongling granites during metamorphism and hydrothermal alteration.

peraluminous Nage granites, the Gangbian Alkaline Complex and the Zhenzhushan, Huangshan and Meiling bimodal volcanic rocks (Li et al., 2008b, 2010a, 2010b; Lyu et al., 2017; Wu et al., 2018) (Fig. 1). On the other hand, the sporadically distributed ~850 Ma bimodal volcanic rocks in the Jiangnan Orogenic Belt are not a definitive indicator of continental rifting or plume-related regional extensional settings. Several present-day and ancient bimodal volcanic associations, such as the Villarrica-Lanin volcanic chain in the Andes (Hickey-Vargas et al., 1989) and the Estancia Glencross Area volcanic rocks in the southernmost South America (D'Orazio et al., 2001) and the Neoproterozoic Sindreth and Punagarh volcanic rocks in Malani igneous Suite in northwest India (Wang et al., 2017, 2018b), were formed in an extensional setting within convergent continental margin. Some A-type granites were also formed at covergent continental margin, including the early Carboniferous K-feldspar granites in northern Tibetan Plateau (Liu et al., 2018), the granitic gneisses of the North Lhasa terrane (Hu et al., 2018) and the ca. 830 Ma felsic volcanic rocks in the eastern Jiangnan Orogen (Li et al., 2016).

The SSZ-type Fuchuan Ophiolite in the eastern Jiangnan Orogenic Belt was formed at 850–820 Ma in a setting similar to the modern Izu-Bonin-Mariana trench-arc-basin system in the western Pacfic, the latter associated with extension within a back-arc basin (Zhang et al., 2012, 2013). Widely distributed 840–815 Ma igneous rocks, such as the 830 Ma high-Mg basalts and diorites in the Sibao and Yiyang region (Chen et al., 2014a; Zhao and Zhou, 2013) and the 830–815 Ma Fanjingshan mafic-ultramafic rocks (Wang et al., 2014; Zhou et al., 2009), are tightly associatd with slab suduction. On the other hand, numerous S-type granite plutons, emplaced during 835–800 Ma in the southeastern Yangtze Block are associated with collision setting (Yao et al., 2014; Zhao et al., 2013). Moreover, the presumably Mesoproterozoic sedimentary basement in the southeastern Yangtze Block has now been precisely dated to 840–810 Ma and a subduction setting such as back-arc and/or retro-arc foreland basin has been interpreted (Wang et al., 2008, 2012, 2013; Zhang et al., 2017; Zhou et al., 2009). Continued subduction of the oceanic crust induced back-arc extension in the southeastern Yangtze margin only after ~850 Ma and consequently, the

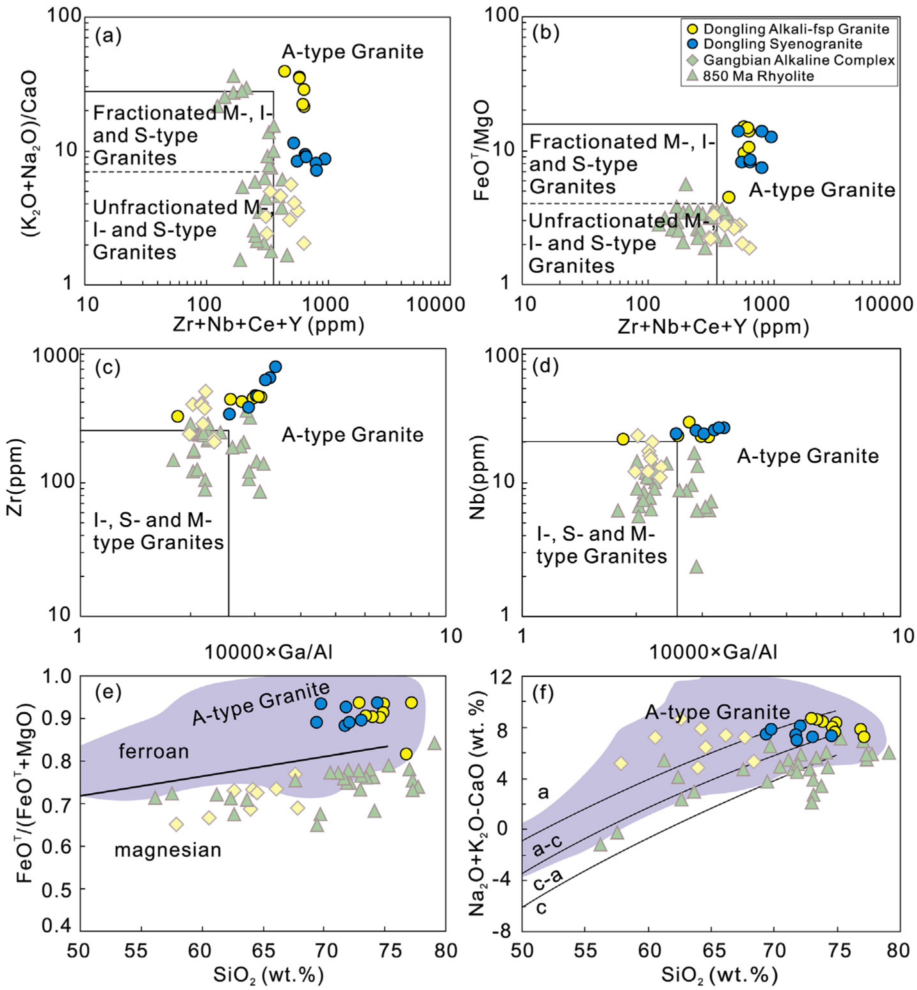

Fig. 9. Discrimination diagrams for A-type granites of the eastern Jiangnan Orogenic Belt (after Whalen et al. (1987) and Frost et al. (2001)). The Gangbian Alkaline Complex and 850 Ma rhyolite data are from Li et al. (2010a, 2010b) and Lyu et al. (2017).

Neoproterozoic amalgamation in the South China Block did not have any linkage with global Grenvillian orogenesis.

In view of the above mentioned synthesis, the Neoproterozoic tectonic evolution of the Jiangnan Orogenic Belt is proposed as below and illustrated in Fig. 14:

1) Convergence of the oceanic-oceanic plates in the southeast (present orientation) of the Yangtze Block resulted in formation of the Shuangxiwu arc at ca. 1000–880 Ma (Li et al., 2009) (Fig. 14a). Leucogranitic lenses within the Northeast Jiangxi Ophiolite suggest that ophiolite was emplaced at ca. 880 Ma, coeval with the amalgamation of Shuangxiwu arc and the Yangtze Block (Li et al., 2008a) (Fig. 14b).
2) Absence of the 880–870 Ma continental-arc related magmatic rocks suggests that the subduction of the oceanic crust had ceased by then. However, there are a number of ca. 850 Ma igneous rocks in the southeasten Jiannnan Orogenic Belt, such as bimodal volcanic rocks (Lyu et al., 2017), Gangbian Alkaline Complex (Li et al., 2010b), strongly peraluminous Nage granites (Wu et al., 2018) and A-type

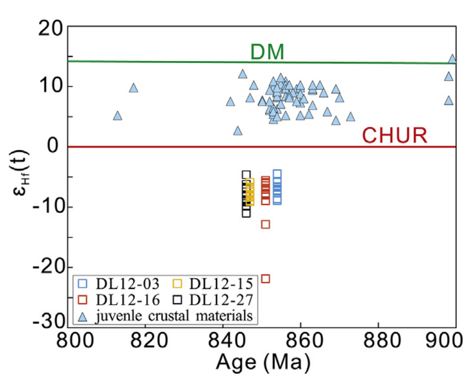

Fig. 10. Plots of $\varepsilon_{Hf}(t)$ versus zircon U—Pb ages. The magmatic zircon data of the juvenile crust are from Yao et al. (2014, 2015).

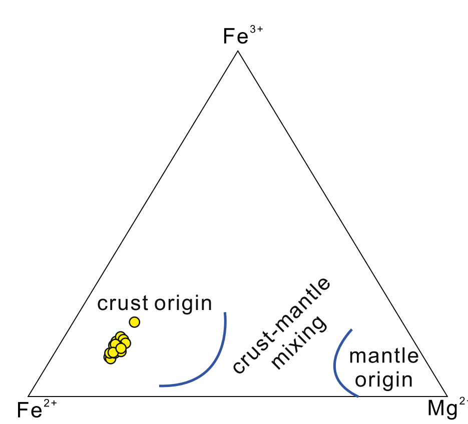

Fig. 11. Plots of $Fe^{3+} - Fe^{2+} - Mg^{2+}$ triangular diagram of biotite chemical compositions of Dongling granites for material origin.

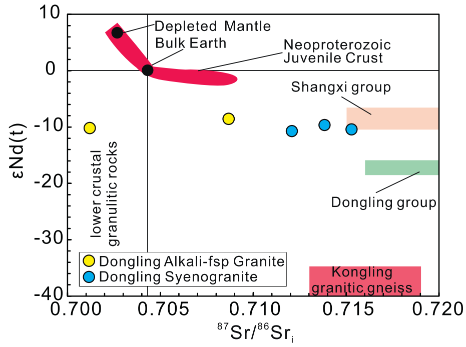

Fig. 12. Initial $^{87}Sr/^{86}Sr$ versus $\varepsilon_{Nd}(t)$ ($t = 850$ Ma) diagram of the Dongling granites. The Kongling granitic gneiss, Shangxi Group, Dongling Group and the Neoproterozoic juvenile crust Sr—Nd isotopes data are from Chen et al. (2001), Wu et al. (2006) and Gao et al. (2009).

granites (present study), related to the break-off regime of the previously subducted oceanic crust (Fig. 14c).

3) Voluminous 840–820 Ma magmatic rocks (mafic to felsic) and 840–815 Ma sedimentary deposits (Sibao Group and its equivalents) from the southeastern part of the Yangtze Block represent a back-arc basin setting, suggesting that the oceanic crust subducted again after 850 Ma (Fig. 14d), therefore collision between Yangtze and Cathaysia blocks should be later than 850 Ma.

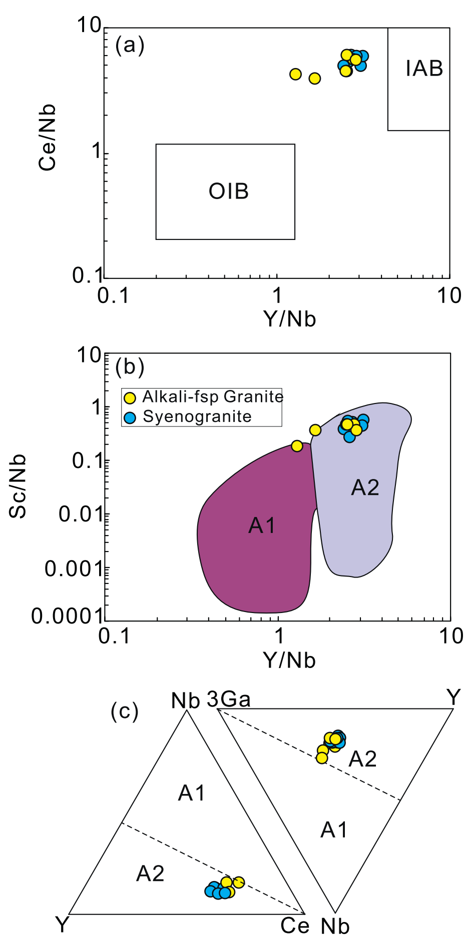

Fig. 13. (a) Ce/Nb versus Y/Nb, (b) Sc/Nb versus Y/Nb and (c) representative trivariate plots for Dongling A-type granites. IAB: island arc basalts; OIB: oceanic island basalts. Dashed line corresponds to Y/Nb ratio of 1.2 (after Eby, 1992).

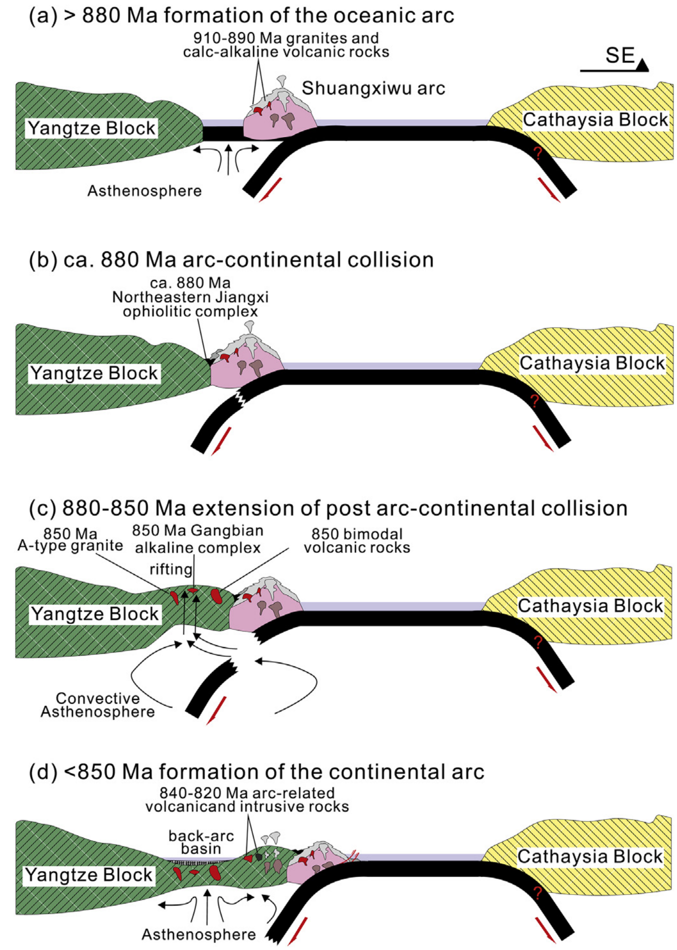

Fig. 14. Simplified model showing Neoproterozoic tectonic evolution of the South China Block. (a) The Shuangxiwu arc formation by northwestward subduction of oceanic crust > 880 Ma; (b) The Shuangxiwu arc collision with Yangtze Block and the subducting oceanic crust break-off at ca. 880 Ma; (c) Extension of post arc-continental collision resulting from the subducting oceanic crust break-off during 880–850 Ma; (d) The oceanic crust from the Cathaysia Block resuming subduction post 850 Ma resulting in the formation of the continental arc in the southeastern Yangtze Block.

6. Conclusions

1) The Dongling A-type granites in eastern Jiangnan Orogenic Belt, South China, were emplaced at ca. 850 Ma, as established by LA-ICP-MS zircon U—Pb geochronology.
2) The Dongling A-type granites were generated by melting of a granulitic metasedimentary source after a previous melt extraction, at low pressure and high temperature.
3) The Dongling A-type granites formed in a rift setting resulting from the subduction slab break-off at 880–850 Ma. Resumption of subduction of oceanic crust after ~850 Ma resulted in emplacement of arc-related magmatic rocks and sedimentation.

Supplementary data to this article can be found online at https://doi.org/10.1016/j.lithos.2018.08.016.

Acknowledgements

This study was supported by the National Natural Science Foundation of China (NSFC 41572170), “Thousand Youth Talents Plan” grant to Wei Wang, Fundamental Research Funds for the Central Universities, China University of Geosciences (Wuhan) (CUGGJ1709) and MOST Special Fund from the State Key Laboratory of Geological Processes and Mineral Resources (MSFGPMR 01-1). We would like to thank Jean

Wong for LA-(MC)-ICPMS analyses, Xiao Fu, Liang Qi and Kejun Hou for whole rock elemental and isotopic analyses. Jun Liu, Zerui Liu and Zhixin Han are thanked for their generous help during field work. Constructive comments from three anonymous reviewers and Editor Nelson Eby are thanked to improve the presentation and interpretation significantly.

References

Andersen, T., 2002. Correction of common lead in U-Pb analyses that do not report ^{204}Pb. Chem. Geol. 192, 59–79.

Anderson, J.L., Thomas, W.M., 1985. Proterozoic anorogenic two-mica granites: Silver Plume and St. Vrain batholiths of Colorado. Geology 13, 177–180.

Bea, F., Montero, P., 1999. Behavior of accessory phases and redistribution of Zr, REE, Y, Th, and U during metamorphism and partial melting of metapelites in the lower crust: an example from the Kinzigite Formation of Ivrea-Verbano, NW Italy. Geochim. Cosmochim. Acta 63, 1133–1153.

BGMRAP (Bureau of Geology and Mineral Resource of Anhui Province), 1987. Regional Geology of Anhui Province. Geological Publishing, Beijing (in Chinese with English abstract).

Blichert-Toft, J., Albarède, F., 1998. The Lu-Hf isotope geochemistry of chondrites and the evolution of the mantle-crust system. Earth Planet. Sci. Lett. 154, 243–258.

Bonin, B., 2007. A-type granites and related rocks: Evolution of a concept, problems and prospects. Lithos 97, 1–29.

Chen, J.F., 1991. Magmatism along the southeast margin of the Yangtze block: Precambrian collision of the Yangtze and Cathaysia blocks of China. Geology 19, 815–818.

Chen, Z.H., Xing, G.F., 2016. Geochemical and zircon U-Pb-Hf-O isotopic evidence for a coherent Paleoproterozoic basement beneath the Yangtze Block, South China. Precambrian Res. 279, 81–90.

Chen, J.F., Yan, J., Xie, Z., Xu, X., Xing, F., 2001. Nd and Sr isotopic compositions of igneous rocks from the Lower Yangtze region in eastern China: constraints on sources. Physics and Chemistry of the Earth, Part A: Solid Earth and Geodesy 26, 719–731.

Chen, F.K., Zhu, X.Y., Wang, W., Wang, F., Hieu, P., Siebel, W., 2009. Single-grain detrital muscovite Rb-Sr isotopic composition as an indicator of provenance for the Carboniferous sedimentary rocks in northern Dabie, China. Geochem. J. 43, 257–273.

Chen, W.T., Sun, W.H., Wang, W., Zhao, J.H., Zhou, M.F., 2014. "Grenvillian" intra-plate mafic magmatism in the southwestern Yangtze Block, SW China. Precambrian Res. 242, 138–153.

Chen, X., Wang, D., Wang, X.L., Gao, J.F., Shu, X.J., Zhou, J.C., Qi, L., 2014a. Neoproterozoic chromite-bearing high-Mg diorites in the western part of the Jiangnan orogen, southern China: Geochemistry, petrogenesis and tectonic implications. Lithos 200-201, 35–48.

Chu, Y., Faure, M., Lin, W., Ji, W., 2012a. Tectonics of the Middle Triassic intracontinental Xuefengshan Belt, South China: new insights from structural and chronological constraints on the basal décollement zone. Int. J. Earth Sci. 101, 2125–2150.

Chu, Y., Lin, W., Faure, M., Wang, Q., Ji, W., 2012b. Phanerozoic tectonothermal events of the Xuefengshan Belt, central South China: Implications from U-Pb age and Lu-Hf determinations of granites. Lithos 150, 243–255.

Clemens, A., 1990. The granulite-granite connection. In: Vielzeuf, D., Vidal, P. (Eds.), Granulites and Crustal Evolution. Kluwer, Dordrecht, pp. 25–36.

Clemens, J.D., Holloway, J.R., White, A.J.R., 1986. Origin of an A-type granites: Experimental constrains. Am. Mineral. 71, 317–324.

Collins, W.J., Beams, S.D., White, A.J.R., Chappell, B.W., 1982. Nature and origin of A-type granites with particular reference to southeastern Australia. Contrib. Mineral. Petrol. 80, 189–200.

Creaser, R.A., Price, R.C., Wormald, R.J., 1991. A-type granites revisited: Assessment of a residual-source model. Geology 19, 163.

Cui, X., Zhu, W., Fitzsimons, I.C.W., Wang, X., Lu, Y., Wu, X., 2017. A possible transition from island arc to continental arc magmatism in the eastern Jiangnan Orogen, South China: Insights from a Neoproterozoic (870 - 860 Ma) gabbroic-dioritic complex near the Fuchuan ophiolite. Gondwana Res. 46, 1–16.

Dall'Agnol, R., Scaillet, B., Pichavant, M., 1999. An experimental study of a lower proterozoic A-type granite from the Eastern Amazonian Craton, Brazil. J. Petrol. 40, 1673–1698.

Dong, S., Qiu, R., 1993. The Tecctonics and Magmatism in the Yueshan Area, Anqing. Geological Publishing, Beijing (in Chinese with English abstract).

Dong, Y., Zhang, G., Neubauer, F., Liu, X., Christoph, H., Zhou, D., Li, W., 2011. Syn- and post-collisional granitoids in the Central Tianshan orogen: Geochemistry, geochronology and implications for tectonic evolution. Gondwana Res. 20, 568–581.

D'Orazio, M., Agostini, S., Innocenti, F., Haller, M.J., Manetti, P., Mazzarini, F., 2001. Slab window-related magmatism from southernmost South America: the Late Miocene mafic volcanics from the Estancia Glencross Area (~52° S, Argentina-Chile). Lithos 57, 67–89.

Eby, G.N., 1990. The A-type granitoids: A review of their occurrence and chemical characteristics and speculations on their petrogenesis. Lithos 26, 115–134.

Eby, G.N., 1992. Chemical subdivision of the A-type granitoids: Petrogenetic and tectonic implications. Geology 20, 641–644.

Eby, G.N., Kochhar, N., 1990. Geochemistry and petrogenesis of the Malani igneous suite, North Peninsular India. J. Geol. Soc. India 36, 109–130.

Feng, S.J., Zhao, K.D., Ling, H.F., Chen, P.R., Chen, W.F., Sun, T., Jiang, S.Y., Pu, W., 2014. Geochronology, elemental and Nd-Hf isotopic geochemistry of Devonian A-type granites in central Jiangxi, South China: Constraints on petrogenesis and post-collisional extension of the Wuyi-Yunkai orogeny. Lithos 206-207, 1–18.

Frost, C.D., Frost, B.R., 1997. Reduced rapakivi-type granites: The tholeiite connection. Geology 25, 647–650.

Frost, C.D., Frost, B.R., Chamberlain, K.R., Edwards, B.R., 1999. Petrogenesis of the 1.43 Ga Sherman Batholith, SE Wyoming, USA: a Reduced, Rapakivi-type Anorogenic Granite. J. Petrol. 40, 1771–1802.

Frost, B.R., Barnes, C.G., Collins, W.J., Arculus, R.J., Ellis, D.J., Frost, C.D., 2001. A Geochemical Classification for Granitic Rocks. J. Petrol. 42, 2033–2048.

Gao, J., Klemd, R., Long, L., Xiong, X., Qian, Q., 2009. Adakitic signature formed by fractional crystallization: An interpretation for the Neo-Proterozoic meta-plagiogranites of the NE Jiangxi ophiolitic mélange belt, South China. Lithos 110, 277–293.

Gao, S., Yang, J., Zhou, L., Li, M., Hu, Z.C., Guo, J.L., Yuan, H.L., Gong, H.J., Xiao, G.Q., Wei, J.Q., 2011. Age and growth of the Archean Kongling terrain, South China, with emphasis on 3.3 Ga granitoid gneisses. Am. J. Sci. 311, 153–182.

Griffin, W.L., Wang, X., Jackson, S.E., Pearson, N.J., O'Reilly, S.Y., Xu, X., Zhou, X., 2002. Zircon chemistry and magma mixing, SE China: In-situ analysis of Hf isotopes, Tonglu and Pingtan igneous complexes. Lithos 61, 237–269.

Grimmer, J.C., Ratschbacher, L., McWilliams, M., Franz, L., Gaitzsch, I., Tichomirowa, M., Hacker, B.R., Zhang, Y., 2003. When did the ultrahigh-pressure rocks reach the surface? A ^{207}Pb/^{206}Pb zircon, ^{40}Ar/^{39}Ar white mica, Si-in-white mica, single-grain provenance study of Dabie Shan synorogenic foreland sediments. Chem. Geol. 197, 87–110.

Guo, J.L., Gao, S., Wu, Y.B., Li, M., Chen, K., Hu, Z.C., Liang, Z.W., Liu, Y.S., Zhou, L., Zong, K.Q., Zhang, W., Chen, H.H., 2014. 3.45 Ga granitic gneisses from the Yangtze Craton, South China: Implications for Early Archean crustal growth. Precambrian Res. 242, 82–95.

Han, Q., Peng, S., Kusky, T., Polat, A., Jiang, X., Cen, Y., Liu, S., Deng, H., 2017. A Paleoproterozoic ophiolitic mélange, Yangtze craton, South China: Evidence for Paleoproterozoic suturing and microcontinent amalgamation. Precambrian Res. 293, 13–38.

Henry, D., Guidotti, C., Thomson, J., 2005. The Ti-saturation surface for low-to-medium pressure metapelitic biotites: Implications for geothermometry and Ti-substitution mechanisms. Am. Mineral. 90, 316–328.

Hickey-Vargas, R., Roa, H.M., Escobar, L.L., Frey, F.A., 1989. Geochemical variations in Andean basaltic and silicic lavas from the Villarrica-Lanin volcanic chain (39.5° S): an evaluation of source heterogeneity, fractional crystallization and crustal assimilation. Contrib. Mineral. Petrol. 103, 361–386.

Hu, P.Y., Zhai, Q.G., Wang, J., Tang, Y., Wang, H.T., Hou, K.J., 2018. Precambrian origin of the North Lhasa terrane, Tibetan Plateau: Constraint from early Cryogenian back-arc magmatism. Precambrian Res. 313, 51–67.

Huang, S.F., Wang, W., 2018. The origin of the Fanjingshan mafic-ultramafic rocks, western Jiangnan Orogen, South China: implications for PGE fractionation and mineralization. J. Earth Sci. https://doi.org/10.1007/s12583-018-0984-0.

Jackson, S.E., Pearson, N.J., Griffin, W.L., Belousova, E.A., 2004. The application of laser ablation-inductively coupled plasma-mass spectrometry to in situ U-Pb zircon geochronology. Chem. Geol. 211, 47–69.

Jung, S., Pfander, J.A., 2007. Source composition and melting temperatures of orogenic granitoids: constraints from CaO/Na_2O, Al_2O_3/TiO_2 and accessory mineral saturation thermometry. Eur. J. Mineral. 19, 859–870.

Kemp, T., Paterson, B., Hawkesworth, C., 2005. A coupled Lu-Hf and O isotope in zircon approach to granite genesis. Geochim. Cosmochim. Acta 69 (Supplement), A243.

King, P.L., White, A.J.R., Chappell, B.W., Allen, C.M., 1997. Characterization and origin of aluminous A-type granites from the lachlan fold belt, Southeastern Australia. J. Petrol. 38, 371–391.

Klimm, K., Holtz, F., Johannes, W., King, P.L., 2003. Fractionation of metaluminous A-type granites: an experimental study of the Wangrah Suite, Lachlan Fold Belt, Australia. Precambrian Res. 124, 327–341.

Klimm, K., Holtz, F., King, P.L., 2008. Fractionation vs. magma mixing in the Wangrah Suite A-type granites, Lachlan Fold Belt, Australia: experimental constraints. Lithos 102, 415–434.

Li, Z.X., Li, X.H., Kinny, P.D., Wang, J., Zhang, S., Zhou, H.W., 2003. Geochronology of Neoproterozoic syn-rift magmatism in the Yangtze Craton, South China and correlations with other continents: evidence for a mantle superplume that broke up Rodinia. Precambrian Res. 122, 85–109.

Li, W.X., Li, X.H., Li, Z.X., Lou, F.S., 2008a. Obduction-type granites within the NE Jiangxi Ophiolite: Implications for the final amalgamation between the Yangtze and Cathaysia Blocks. Gondwana Res. 13, 288–301.

Li, X.H., Li, W.X., Li, Z.X., Liu, Y., 2008b. 850 - 790 Ma bimodal volcanic and intrusive rocks in northern Zhejiang, South China: A major episode of continental rift magmatism during the breakup of Rodinia. Lithos 102, 341–357.

Li, X.H., Wang, X.C., Li, W.X., Li, Z.X., 2008c. Petrogenesis and tectonic significance of Neoproterozoic basaltic rocks in South China: From orogenesis to intracontinental rifting. Geochimica 37, 382–398.

Li, X.H., Li, W.X., Li, Z.X., Lo, C.H., Wang, J., Ye, M.F., Yang, Y.H., 2009. Amalgamation between the Yangtze and Cathaysia Blocks in South China: constraints from SHRIMP U-Pb zircon ages, geochemistry and Nd-Hf isotopes of the Shuangxiwu volcanic rocks. Precambrian Res. 174, 117–128.

Li, W.X., Li, X.H., Li, Z.X., 2010a. Ca. 850 Ma Bimodal Volcanic Rocks in Northeastern Jiangxi Province, South China: Initial Extension During the Breakup of Rodinia? Am. J. Sci. 310, 951–980.

Li, X.H., Li, W.X., Li, Q.L., Wang, X.C., Liu, Y., Yang, Y.H., 2010b. Petrogenesis and tectonic significance of the ~850 Ma Gangbian alkaline complex in South China: Evidence from in situ zircon U-Pb dating, Hf-O isotopes and whole-rock geochemistry. Lithos 114, 1–15.

Li, Z.X., Li, X.H., Wartho, J.A., Clark, C., Li, W.X., Zhang, C.L., Bao, C., 2010c. Magmatic and metamorphic events during the early Paleozoic Wuyi-Yunkai orogeny, southeastern South China: New age constraints and pressure-temperature conditions. Geol. Soc. Am. Bull. 122, 772–793.

Li, H., Zhang, H., Ling, M.X., Wang, F.Y., Ding, X., Zhou, J.B., Yang, X.Y., Tu, X.L., Sun, W.D., 2011. Geochemical and zircon U-Pb study of the Huangmeijian A-type granite:

implications for geological evolution of the Lower Yangtze River belt. Int. Geol. Rev. 53, 499–525.
Li, L.M., Lin, S.F., Xing, G.F., Davis, D.W., Davis, W.J., Xiao, W.J., Yin, C.Q., 2013. Geochronology and geochemistry of volcanic rocks from the Shaojiwa Formation and Xingzi Group, Lushan area, SE China: Implications for Neoproterozoic back-arc basin in the Yangtze Block. Precambrian Res. 238, 1–17.
Li, L.M., Lin, S.F., Xing, G.F., Davis, D.W., Jiang, Y., Davis, W., Zhang, Y., 2016. Ca. 830 Ma back-arc type volcanic rocks in the eastern part of the Jiangnan orogen: Implications for the Neoproterozoic tectonic evolution of South China Block. Precambrian Res. 275, 209–224.
Liu, H., Zhao, J.H., 2018. Neoproterozoic peraluminous granitoids in the Jiangnan Fold Belt: Implications for lithospheric differentiation and crustal growth. Precambrian Res. 309, 152–165.
Liu, Y.S., Gao, S., Hu, Z.C., Gao, C.G., Zong, K.Q., Wang, D.B., 2010. Continental and Oceanic Crust Recycling-induced Melt-Peridotite Interactions in the Trans-North China Orogen: U-Pb Dating, Hf Isotopes and Trace Elements in Zircons from Mantle Xenoliths. J. Petrol. 51, 537–571.
Liu, Z., Jiang, Y.H., Wang, G.C., Ni, C.Y., Qing, L., Zhang, Q., 2015. Middle Neoproterozoic (~845 Ma) continental arc magmatism along the northwest side of the Jiangshan-Shaoxing suture, South China: Geochronology, geochemistry, petrogenesis and tectonic implications. Precambrian Res. 268, 212–226.
Liu, J.H., Xie, C.M., Li, C., Wang, M., Wu, H., Li, X.K., Liu, Y.M., Zhang, T.Y., 2018. Early Carboniferous adakite-like and I-type granites in central Qiangtang, northern Tibet: Implications for intra-oceanic subduction and back-arc basin formation within the Paleo-Tethys Ocean. Lithos 296-299, 265–280.
Ludwig, K.R., 2003. User's Manual for Isoplot 3.00, a Geolochronolgical Toolkit for Microsoft Excel. vol. 4. Berkeley Geochronology Center, Special Publication, pp. 25–32.
Lyu, P.L., Li, W.X., Wang, X.C., Pang, C.J., Cheng, J.X., Li, X.H., 2017. Initial breakup of supercontinent Rodinia as recorded by ca 860 - 840 Ma bimodal volcanism along the southeastern margin of the Yangtze Block, South China. Precambrian Res. 296, 148–167.
Middlemost, E.A.K., 1994. Naming materials in the magma/igneous rock system. Earth-Science Reviews 37, 215–224.
Miller, C.F., McDowell, S.M., Mapes, R.W., 2003. Hot and cold granites? Implications of zircon saturation temperatures and preservation of inheritance. Geology 31, 529–532.
Min, S., Chen, N.S., Zhao, G.C., Wilde, S.A., Ye, K., Guo, J.H., Chen, Y., Yuan, C., 2008. U-Pb zircon and Sm-Nd isotopic study of the Huangtuling granulite, Dabie-Sulu belt, China: Implication for the paleoproterozoic tectonic history of the Yangtze Craton. Am. J. Sci. 308, 469–483.
Patiño Douce, A.E., 1997. Generation of metaluminous A-type granites by low-pressure melting of calc-alkaline granitoids. Geology 25, 743–746.
Patiño Douce, A.E., Beard, J.S., 1995. Dehydration-melting of Biotite Gneiss and Quartz Amphibolite from 3 to 15 kbar. J. Petrol. 36, 707–738.
Patiño Douce, A.E., Beard, J.S., 1996. Effects of *P*, *f*(O2) and Mg/Fe Ratio on Dehydration Melting of Model Metagreywackes. J. Petrol. 37, 999–1024.
Pearce, J.A., Peate, D.W., 1995. Tectonic Implications of the Composition of Volcanic ARC Magmas. Annu. Rev. Earth Planet. Sci. 23, 251–285.
Polat, A., Hofmann, A.W., Rosing, M.T., 2002. Boninite-like volcanic rocks in the 3.7 - 3.8 Ga Isua greenstone belt, West Greenland: geochemical evidence for intra-oceanic subduction zone processes in the early Earth. Chem. Geol. 184, 231–254.
Qi, L., Hu, J., Gregoire, D.C., 2000. Determination of trace elements in granites by inductively coupled plasma mass spectrometry. Talanta 51, 507–513.
Qiu, Y.M., Gao, S., McNaughton, N.J., Groves, D.I., Ling, W., 2000. First evidence of > 3.2 Ga continental crust in the Yangtze craton of south China and its implications for Archean crustal evolution and Phanerozoic tectonics. Geology 28, 11–14.
Qiu, L., Tan, D.P., Tang, S.L., Yang, W.Q., Tang, W.X., Wang, X., 2016. Mesozoic geology of southwestern China: Indosinian foreland overthrusting and subsequent deformation. J. Asian Earth Sci. 122, 91–105.
Rudnick, R.L., Gao, S., 2003. Composition of the continental crust. Treatise on Geochemistry 3, 1–64.
Skjerlie, K.P., Johnston, A.D., 1992. Vapor-absent melting at 10 kbar of a biotite- and amphibole-bearing tonalitic gneiss: Implications for the generation of A-type granites. Geology 20, 263–266.
Söderlund, U., Patchett, P.J., Vervoort, J.D., Isachsen, C.E., 2004. The ^{176}Lu decay constant determined by Lu-Hf and U-Pb isotope systematics of Precambrian mafic intrusions. Earth Planet. Sci. Lett. 219, 311–324.
Streckeisen, A., Maitre, R.W.L., 1979. A chemical approximation to the modal QAPF classification of the igneous rocks. Neues Jahrbuch Miner. 136, 169–206.
Su, J., Zhang, Y.Q., Dong, S.W., Chen, X., Li, Y., Cui, J., 2014. Geochronology and Hf Isotopes of Granite Gravel from Fanjingshan, South China: Implication for the Precambrian Tectonic Evolution of Western Jiangnan Orogen. J. Earth Sci. 25, 619–629.
Sun, M., Chen, N., Zhao, G., Wilde, S.A., Ye, K., Guo, J., Chen, Y., Yuan, C., 2008. U-Pb zircon and Sm-Nd isotopic study of the Huangtuling granulite, Dabie-Sulu belt, China: Implication for the paleoproterozoic tectonic history of the Yangtze Craton. Am. J. Sci. 308, 469–483.
Sun, S.S., McDonough, W.F., 1989. Chemical and isotopic systematics of oceanic basalts: implications for mantle composition and processes. Geological Society of London, Special Publication 42, 313–345.
Sun, W.H., Zhou, M.F., Gao, J.F., Yang, Y.H., Zhao, X.F., Zhao, J.H., 2009. Detrital zircon U-Pb geochronological and Lu-Hf isotopic constraints on the Precambrian magmatic and crustal evolution of the western Yangtze Block, SW China. Precambrian Res. 172, 99–126.
Sun, J., Shu, L.S., Santosh, M., Wamg, L., 2017. Neoproterozoic tectonic evolution of the Jiuling terrane in the central Jiangnan orogenic belt (South China): constraints from magmatic suites. Precambrian Res. 302, 279–297.
Sylvester, P.J., 1998. Post-collisional strongly peraluminous granites. Lithos 45, 29–44.
Turner, S.P., Foden, J.D., Morrison, R.S., 1992. Derivation of some A-type magmas by fractionation of basaltic magma: an example from the Padthaway Ridge, South Australia. Lithos 28, 151–179.
Uchida, E., Endo, S., Makino, M., 2007. Relationship between solidification depth of granitic rocks and formation of hydrothermal ore deposits. Resour. Geol. 57, 47–56.
Wang, J., Li, Z.X., 2003. History of Neoproterozoic rift basins in South China: implications for Rodinia break-up. Precambrian Res. 122, 141–158.
Wang, X.L., Zhou, J.C., Qiu, J.S., Zhang, W.L., Liu, X.M., Zhang, G.L., 2006. LA-ICP-MS U-Pb zircon geochronology of the Neoproterozoic igneous rocks from Northern Guangxi, South China: Implications for tectonic evolution. Precambrian Res. 145, 111–130.
Wang, X.L., Zhao, G.C., Zhou, J.C., Liu, Y.S., Hu, J., 2008. Geochronology and Hf isotopes of zircon from volcanic rocks of the Shuangqiaoshan Group, South China: Implications for the Neoproterozoic tectonic evolution of the eastern Jiangnan orogen. Gondwana Res. 14, 355–367.
Wang, Q., Wyman, D.A., Li, Z.X., Bao, Z.W., Zhao, Z.H., Wang, Y.X., Jian, P., Yang, Y.H., Chen, L.L., 2010. Petrology, geochronology and geochemistry of ca. 780 Ma A-type granites in South China: Petrogenesis and implications for crustal growth during the breakup of the supercontinent Rodinia. Precambrian Res. 178, 185–208.
Wang, W., Zhou, M.F., 2014. Provenance and tectonic setting of the Paleo- to Mesoproterozoic Dongchuan Group in the southwestern Yangtze Block, South China: Implication for the breakup of the supercontinent Columbia. Tectonophysics 610, 110–127.
Wang, W., Zhou, M.F., Yan, D.P., Li, J.W., 2012. Depositional age, provenance, and tectonic setting of the Neoproterozoic Sibao Group, southeastern Yangtze Block, South China. Precambrian Res. 192-195, 107–124.
Wang, W., Zhou, M.F., Yan, D.P., Li, L., Malpas, J., 2013. Detrital zircon record of Neoproterozoic active-margin sedimentation in the eastern Jiangnan Orogen, South China. Precambrian Res. 235, 1–19.
Wang, W., Zhao, J.H., Zhou, M.F., Yang, S.H., Chen, F.K., 2014. Neoproterozoic Mafic-Ultramafic Intrusions from the Fanjingshan Region, South China: Implications for Subduction-Related Magmatism in the Jiangnan Fold Belt. J. Geol. 122, 455–473.
Wang, X.L., Zhou, J.C., Griffin, W.L., Zhao, G.C., Yu, J.H., Qiu, J.S., Zhang, Y.J., Xing, G.F., 2014a. Geochemical zonation across a Neoproterozoic orogenic belt: Isotopic evidence from granitoids and metasedimentary rocks of the Jiangnan orogen, China. Precambrian Res. 242, 154–171.
Wang, J., Zhou, X., Deng, Q., Fu, X., Duan, T., Guo, X., 2015. Sedimentary successions and the onset of the Neoproterozoic Jiangnan sub-basin in the Nanhua rift, South China. Int. J. Earth Sci. 104, 521–539.
Wang, W., Cawood, P.A., Zhou, M.F., Pandit, M.K., Xia, X.P., Zhao, J.H., 2017. Low-δ^{18}O rhyolites from the Malani Igneous Suite: a positive test for South China and NW India linkage in Rodinia. Geophys. Res. Lett. 44, 10298–10305.
Wang, Y.J., Gan, C.S., Tan, Q.L., Zhang, Y.Z., He, H.Y., Qian, X., Zhang, Y.H., 2018a. Early Neoproterozoic (~840 Ma) slab window in South China: Key magmatic records in the Chencai Complex. Precambrian Res. 314, 434–451.
Wang, W., Pandit, M.K., Zhao, J.H., Chen, W.T., Zheng, J.P., 2018b. Slab break-off triggered lithosphere-asthenosphere interaction at a convergent margin: The Neoproterozoic bimodal magmatism in NW India. Lithos 296 (299), 281–296.
Watson, E.B., Harrison, T.M., 1983. Zircon saturation revisited: temperature and composition effects in a variety of crustal magma types. Earth Planet. Lett. 64, 295–304.
Whalen, J.B., Currie, K.L., Chappell, B.W., 1987. A-type granites: geochemical characteristics, discrimination and petrogenesis. Contrib. Mineral. Petrol. 95, 407–419.
Wu, R.X., Zheng, Y.F., Wu, Y.B., Zhao, Z.F., Zhang, S.B., Liu, X., Wu, F.Y., 2006. Reworking of juvenile crust: Element and isotope evidence from Neoproterozoic granodiorite in South China. Precambrian Res. 146, 179–212.
Wu, T., Zhou, J.X., Wang, X.C., Li, W.X., Wilde, S.A., Sun, H.R., Wang, J.S., Li, Z., 2018. Identification of ca. 850 Ma high-temperature strongly peraluminous granitoids in southeastern Guizhou Province, South China: A result of early extension along the southern margin of the Yangtze Block. Precambrian Res. 308, 18–34.
Xia, Y., Xu, X., Niu, Y., Liu, L., 2018. Neoproterozoic amalgamation between Yangtze and Cathaysia blocks: The magmatism in various tectonic settings and continent-arc-continent collision. Precambrian Res. 309, 56–87.
Xing, F.M., Xu, X., Li, Z.C., 1993. The finding and signifiance of the Paleoproterozoic basement in the middle-lower Yangtze River area. Chin. Sci. Bull. 38, 1883–1886 (in Chinese).
Yan, D.P., Zhou, M.F., Song, H.L., Wang, X.W., Malpas, J., 2003. Origin and tectonic significance of a Mesozoic multi-layer over-thrust system within the Yangtze Block (South China). Tectonophysics 361, 239–254.
Yang, J.H., Wu, F.Y., Chung, S.L., Wilde, S.A., Chu, M.F., 2006. A hybrid origin for the Qianshan A-type granite, northeast China: Geochemical and Sr-Nd-Hf isotopic evidence. Lithos 89, 89–106.
Yao, J.L., Shu, L.S., Santosh, M., 2014. Neoproterozoic arc-trench system and breakup of the South China Craton: Constraints from N-MORB type and arc-related mafic rocks, and anorogenic granite in the Jiangnan orogenic belt. Precambrian Res. 247, 187–207.
Yao, J.L., Shu, L.S., Santosh, M., Li, J.Y., 2015. Neoproterozoic arc-related andesite and orogeny-related unconformity in the eastern Jiangnan orogenic belt: Constraints on the assembly of the Yangtze and Cathaysia blocks in South China. Precambrian Res. 262, 84–100.
Ye, M.F., Li, X.H., Li, W.X., Liu, Y., Li, Z.X., 2007. SHRIMP zircon U-Pb geochronological and whole-rock geochemical evidence for an early Neoproterozoic Sibaoan magmatic arc along the southeastern margin of the Yangtze Block. Gondwana Res. 12, 144–156.
Yin, C.Q., Lin, S.F., Davis, D.W., Zhao, G.C., Xiao, W.J., Li, L.M., He, Y.H., 2013. 2.1 - 1.85 Ga tectonic events in the Yangtze Block, South China: Petrological and geochronological evidence from the Kongling Complex and implications for the reconstruction of supercontinent Columbia. Lithos 182-183, 200–210.

Zhang, R.X., Yang, S.Y., 2016. A Mathematical Model for Determining Carbon Coating Thickness and Its Application in Electron Probe Microanalysis. Microsc. Microanal. 22, 1374–1380.

Zhang, S.B., Zheng, Y.F., 2013. Formation and evolution of Precambrian continental lithosphere in South China. Gondwana Res. 23, 1241–1260.

Zhang, S.B., Wu, R.X., Zheng, Y.F., 2012. Neoproterozoic continental accretion in South China: Geochemical evidence from the Fuchuan ophiolite in the Jiangnan orogen. Precambrian Res. 220-221, 45–64.

Zhang, C.L., Santosh, M., Zou, H.B., Li, H.K., Huang, W.C., 2013. The Fuchuan ophiolite in Jiangnan Orogen: Geochemistry, zircon U-Pb geochronology, Hf isotope and implications for the Neoproterozoic assembly of South China. Lithos 179, 263–274.

Zhang, C.L., Li, H.K., Santosh, M., 2013a. Revisiting the tectonic evolution of South China: interaction between the Rodinia superplume and plate subduction? Terra Nova 25, 212–220.

Zhang, Y.Z., Wang, Y.J., Geng, H.Y., Zhang, Y.H., Fan, W.M., Zhong, H., 2013b. Early Neoproterozoic (~850 Ma) back-arc basin in the Central Jiangnan Orogen (Eastern South China): Geochronological and petrogenetic constraints from meta-basalts. Precambrian Res. 231, 325–342.

Zhang, S.B., He, Q., Zheng, Y.F., 2015a. Geochronological and geochemical evidence for the nature of the Dongling Complex in South China. Precambrian Res. 256, 17–30.

Zhang, Y.Z., Wang, Y., Zhang, Y., Zhang, A., 2015b. Neoproterozoic assembly of the Yangtze and Cathaysia blocks: Evidence from the Cangshuipu Group and associated rocks along the Central Jiangnan Orogen, South China. Precambrian Res. 269, 18–30.

Zhang, F.F., Wang, X.L., Wang, D., Yu, J.H., Zhou, X.H., Sun, Z.M., 2017. Neoproterozoic backarc basin on the southeastern margin of the Yangtze block during Rodinia assembly: New evidence from provenance of detrital zircons and geochemistry of mafic rocks. Geol. Soc. Am. Bull. 129, 904–919.

Zhao, G.C., 2015. Jiangnan Orogen in South China: Developing from divergent double subduction. Gondwana Res. 27, 1173–1180.

Zhao, G.C., Cawood, P.A., 2012. Precambrian geology of China. Precambrian Res. 222-223, 13–54.

Zhao, J.H., Zhou, M.F., 2013. Neoproterozoic high-Mg basalts formed by melting of ambient mantle in South China. Precambrian Res. 233, 193–205.

Zhao, X.F., Zhou, M.F., Li, J.W., Wu, F.Y., 2008. Association of Neoproterozoic A- and I-type granites in South China: Implications for generation of A-type granites in a subduction-related environment. Chem. Geol. 257, 1–15.

Zhao, J.H., Zhou, M.F., Yan, D.P., Zheng, J.P., Li, J.W., 2011. Reappraisal of the ages of Neoproterozoic strata in South China: No connection with the Grenvillian orogeny. Geology 39, 299–302.

Zhao, J.H., Zhou, M.F., Zheng, J.P., 2013. Constraints from zircon U–Pb ages, O and Hf isotopic compositions on the origin of Neoproterozoic peraluminous granitoids from the Jiangnan Fold Belt, South China. Contrib. Mineral. Petrol. 166, 1505–1519.

Zhao, J.H., Pandit, M.K., Wang, W., Xia, X.P., 2018. Neoproterozoic tectonothermal evolution of NW India: Evidence from geochemistry and geochronology of granitoids. Lithos https://doi.org/10.1016/j.lithos.2018.07.020.

Zheng, Q.R., 1983. Calculation of the Fe^{3+} and Fe^{2+} contents in silicate and Ti-Fe oxide minerals from EPMA data. Acta Mineral. Sin. 3, 55–62 (in Chinese with English abstract).

Zheng, Y.F., Wu, R.X., Wu, Y.B., Zhang, S.B., Yuan, H., Wu, F.Y., 2008. Rift melting of juvenile arc-derived crust: Geochemical evidence from Neoproterozoic volcanic and granitic rocks in the Jiangnan Orogen, South China. Precambrian Res. 163, 351–383.

Zheng, Y.F., Xiao, W.J., Zhao, G.C., 2013. Introduction to tectonics of China. Gondwana Res. 23, 1189–1206.

Zhou, M.F., Yan, D.P., Kennedy, A.K., Li, Y., Ding, J., 2002. SHRIMP U-Pb zircon geochronological and geochemical evidence for Neoproterozoic arc-magmatism along the western margin of the Yangtze Block, South China. Earth Planet. Sci. Lett. 196, 51–67.

Zhou, J.C., Wang, X.L., Qiu, J.S., Gao, J.F., 2004. Geochemistry of Meso- and Neoproterozoic mafic-ultramafic rocks from northern Guangxi, China: Arc or plume magmatism? Geochem. J. 38, 139–152.

Zhou, J.C., Wang, X.L., Qiu, J.S., 2009. Geochronology of Neoproterozoic mafic rocks and sandstones from northeastern Guizhou, South China: Coeval arc magmatism and sedimentation. Precambrian Res. 170, 27–42.

Zhou, M.F., Zhao, X.F., Chen, W.T., Li, X.C., Wang, W., Yan, D.P., Qiu, H.N., 2014. Proterozoic Fe-Cu metallogeny and supercontinental cycles of the southwestern Yangtze Block, southern China and northern Vietnam. Earth Sci. Rev. 139, 59–82.

Zhu, G., Xie, C.L., Chen, W., Xiang, B.W., Hu, Z.Q., 2010. Evolution of the Hongzhen metamorphic core complex: Evidence for Early Cretaceous extension in the eastern Yangtze carton, eastern China. Geol. Soc. Am. Bull. 122, 506–516.